Process-evaluation of tropospheric humidity simulated by general circulation models using water vapor isotopic observations: 2. Using isotopic diagnostics to understand the mid and upper tropospheric moist bias in the tropics and subtropics

Camille Risi,[1,2] David Noone,[1] John Worden,[3] Christian Frankenberg,[3] Gabriele Stiller,[4] Michael Kiefer,[4] Bernd Funke,[5] Kaley Walker,[6] Peter Bernath,[7] Matthias Schneider,[4,8] Sandrine Bony,[2] Jeonghoon Lee,[3,9] Derek Brown,[1] and Christophe Sturm[10]

Received 26 July 2011; revised 28 December 2011; accepted 30 December 2011; published 6 March 2012.

[1] Evaluating the representation of processes controlling tropical and subtropical tropospheric relative humidity (RH) in atmospheric general circulation models (GCMs) is crucial to assess the credibility of predicted climate changes. GCMs have long exhibited a moist bias in the tropical and subtropical mid and upper troposphere, which could be due to the mis-representation of cloud processes or of the large-scale circulation, or to excessive diffusion during water vapor transport. The goal of this study is to use observations of the water vapor isotopic ratio to understand the cause of this bias. We compare the three-dimensional distribution of the water vapor isotopic ratio measured from space and ground to that simulated by several versions of the isotopic GCM LMDZ. We show that the combined evaluation of RH and of the water vapor isotopic composition makes it possible to discriminate the most likely cause of RH biases. Models characterized either by an excessive vertical diffusion, an excessive convective detrainment or an underestimated in situ cloud condensation will all produce a moist bias in the free troposphere. However, only an excessive vertical diffusion can lead to a reversed seasonality of the free tropospheric isotopic composition in the subtropics compared to observations. Comparing seven isotopic GCMs suggests that the moist bias found in many GCMs in the mid and upper troposphere most frequently results from an excessive diffusion during vertical water vapor transport. This study demonstrates the added value of water vapor isotopic measurements for interpreting shortcomings in the simulation of RH by climate models.

Citation: Risi, C., et al. (2012), Process-evaluation of tropospheric humidity simulated by general circulation models using water vapor isotopic observations: 2. Using isotopic diagnostics to understand the mid and upper tropospheric moist bias in the tropics and subtropics, *J. Geophys. Res.*, *117*, D05304, doi:10.1029/2011JD016623.

1. Introduction

[2] Despite continuous improvements in climate models, uncertainties in the predicted amplitude of climate change and in the magnitude of underlying feedbacks remain high [*Randall et al.*, 2007]. Because the water vapor feedback constitutes one of the largest positive feedbacks in climate models [*Soden and Held*, 2006], assessing the credibility of predicted relative humidity (RH) changes by atmospheric general circulation models (GCMs) is crucial. In addition, RH strongly impacts the formation of cirrus clouds [*Luo and Rossow*, 2004], boundary layer clouds [*Slingo*, 1980; *Wetzel et al.*, 1996; *Betts*, 2000] and deep convective clouds [*Redelsperger et al.*, 2002; *Derbyshire et al.*, 2004]. Predicting the correct regional changes in RH is thus crucial for a correct prediction of cloud feedbacks, which are still among the largest sources of spread in climate change projections [*Bony and Dufresne*, 2005; *Bony et al.*, 2006]. Therefore, the credibility of simulated climate change depends

[1]Department of Atmospheric and Oceanic Sciences, and Cooperative Institute for Research in Environmental Sciences, University of Colorado at Boulder, Boulder, Colorado, USA.
[2]LMD/IPSL, CNRS, Paris, France.
[3]Jet Propulsion Laboratory, California Institute of Technology, Pasadena, California, USA.
[4]Institute for Meteorology and Climate Research, Karlsruhe Institute of Technology, Karlsruhe, Germany.
[5]Instituto de Astrofisica de Andalucía, Granada, Spain.
[6]Department of Physics, University of Toronto, Toronto, Ontario, Canada.
[7]Department of Chemistry, University of York, York, UK.
[8]CIAI, Agencia Estatal de Meteorología, Santa Cruz de Tenerife, Spain.
[9]Korea Polar Research Institute, Incheon, South Korea.
[10]Department of Geology and Geochemistry, Stockholm University, Stockholm, Sweden.

0148-0227/12/2011JD016623

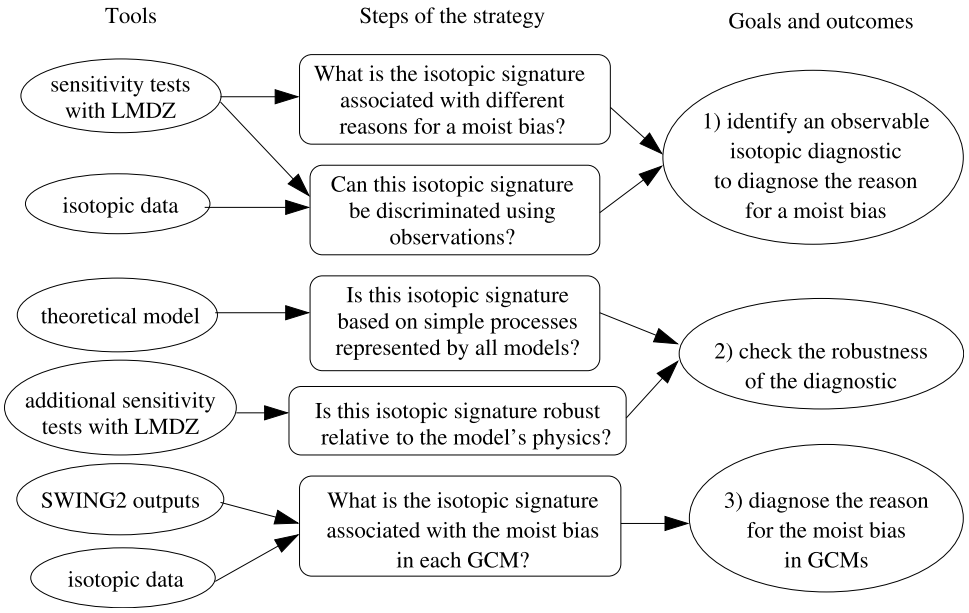

Figure 1. Strategy for developing, testing and applying diagnostics based on the isotopic ratio to identify the cause of the moist bias in models. Rectangles describe the different steps of the strategy used in this paper, and circles explain the tools used at different steps.

on the ability of atmospheric models to correctly simulate the processes that control RH, although no evidence has been shown so far for a systematic relationship between the behavior of models at present and in the future [*John and Soden*, 2007].

[3] Most GCMs exhibit a moist bias in the mid to upper tropical and subtropical troposphere compared to a wide range of data sets [*Soden and Bretherton*, 1994; *Salathe and Chester*, 1995; *Chen et al.*, 1996; *Roca et al.*, 1997; *Chen et al.*, 1998; *Allan et al.*, 2003; *Brogniez et al.*, 2005; *Pierce et al.*, 2006; *John and Soden*, 2007; *Sherwood et al.*, 2010; *Chung et al.*, 2011]. Some of these studies suggest this problem can arise from the parameterization of deep convection [*Chen et al.*, 1996, 1998], others suggest it could be related to an underestimated upper tropospheric large-scale circulation [*Chung et al.*, 2011]. This problem has persisted for more than a decade and questions the capacity of GCMs to accurately represent processes controlling RH. The tropical and subtropical tropospheric RH results from a subtle balance between different processes, among which are large-scale radiative subsidence [e.g., *Sherwood*, 1996; *Schneider et al.*, 2006; *Folkins and Martin*, 2005], detrainment of condensate from convective clouds and its subsequent evaporation [e.g., *Wright et al.*, 2009], evaporation of the falling precipitation [e.g., *Folkins and Martin*, 2005] or lateral mixing [e.g., *Zhang et al.*, 2003]. Therefore, the representation of many processes may potentially contribute to the moist bias. Measurements of humidity alone are not sufficient to diagnose which of this processes are the most likely candidates.

[4] The water vapor stable isotopic composition is affected by fractionation during phase changes. Measurements of water vapor isotopologues therefore provide complementary information on the water budget when combined with humidity because they record the integrated history of phase changes within a given air mass [*Dansgaard*, 1964]. In a companion paper [*Risi et al.*, 2012] (hereafter P1), we have analyzed various data sets (4 satellite, 16 ground-based remote-sensing, 5 surface in situ and 3 aircraft) to document the three-dimensional distribution of the tropospheric water vapor composition and to derive robust characteristics that could be used to evaluate models. For example, we have identified that the δD seasonality in the subtropics and mid latitudes (with higher δD in summer) was a robust characteristic across all data sets and at all tropospheric levels. We have used these data sets to evaluate the isotopic GCM LMDZ and have identified some biases that are robust compared to all data sets, such as the underestimated seasonality in the subtropics. In addition, we have compared 7 GCMs from the SWING2 (Stable Water INtercomparison Group phase) project, and have shown large discrepancies between models regarding important features of the isotopic distribution: meridional gradient, seasonality, and spatial contrasts in the tropics. This suggests that water vapor isotopic measurements could be used to efficiently discriminate models regarding their representation of the processes controlling RH. Further, we have shown that differences in isotopic behavior are not obviously linked to differences in simulated humidity, confirming that water vapor isotopic composition provides additional information compared to humidity measurements. The goal of this paper is thus to exploit the information provided by the combination of water vapor isotopic measurements, to understand the cause of the moist bias in GCMs.

[5] To do so, the approach is illustrated in Figure 1. First, with the isotopic GCM LMDZ, we perform different sensitivity tests that exhibit a moist bias for different causes. From these simulations, we investigate how the different

processes impact the isotopic composition, and how it hurts the agreement with isotopic data sets. This allows us to identify a discriminating diagnostic for the cause of the moist bias that is robust across data sets. Second, we further check the robustness of this diagnostic by creating a theoretical framework to understand the link between the moist bias and isotopic behavior. The framework is used to show that this link can be explained based on simple processes that are represented in all models. We also use additional sensitivity tests to show that the diagnostic does not crucially depend on the model physics. Third, once we have accumulated confidence in the robustness of the diagnostic, we apply it to six other GCMs from the SWING2 project to determine the most frequent cause of the moist bias in models.

[6] We present the LMDZ GCM, the isotopic data sets and the SWING2 database in section 2. We describe the theoretical framework used to interpret the sensitivity tests in section 3. In section 4, we present the sensitivity tests and their impact on RH in section 4. In section 5, we describe the impact of the tests on the water vapor isotopic composition and compare the simulations with the isotopic data. In section 6 we further check its robustness and apply it to SWING2 models. We conclude and propose perspectives for future work in section 7.

2. General Circulation Models and Data Sets

2.1. The LMDZ4 Model and Control Simulation

[7] LMDZ4 (Laboratoire de Météorologie Dynamique-Zoom) [*Hourdin et al.*, 2006] is the atmospheric component of the Institut Pierre-Simon Laplace coupled model: IPSL-CM4 [*Marti et al.*, 2005] used in CMIP3 (Coupled Model Intercomparison Project) [*Meehl et al.*, 2007] and IPSL-CM5A (J.-L. Dufresne et al., Climate change projections using the IPSL-CM5 Earth System Model: from CMIP3 to CMIP5, submitted to *Climate Dynamics*, 2012) used in CMIP5. It is used with a resolution of 2.5° in latitude, 3.75° in longitude and 19 vertical levels. The physical package includes the Emanuel convective scheme [*Emanuel*, 1991; *Emanuel and Zivkovic-Rothman*, 1999], which represents convective systems as an adiabatic updraft, an ensemble of mixed updrafts and downdrafts, and an unsaturated downdraft driven by rain reevaporation. A particular focus had been placed on the parameterization and optimization of microphysical processes, such as the precipitation efficiency ϵ_p representing the proportion of condensate that is converted to precipitation [*Emanuel and Zivkovic-Rothman*, 1999]. Large-scale condensation is represented by a statistical cloud scheme based on the sub-grid-scale distribution of water vapor [*Bony and Emanuel*, 2001]. Water vapor and condensate are advected using a second order monotonic finite volume advection scheme [*Van Leer*, 1977; *Hourdin and Armengaud*, 1999]. The isotopic version of LMDZ is described in detail by *Risi et al.* [2010b].

[8] LMDZ is forced by observed sea surface temperatures (SST) and sea ice following the AMIP (Atmospheric Model Inter-comparison Project) protocol [*Gates*, 1992] from 1978 to 2009. The year 2010 is forced by NCEP (National Center for Environmental Prediction) SSTs [*Kalnay et al.*, 1996] because the AMIP SSTs were not yet available. To facilitate the comparison between simulations and observations on a daily basis, horizontal winds at each vertical level are nudged by ECMWF reanalyses [*Uppala et al.*, 2005] with a relaxation time scale of 1h as in work by *Risi et al.* [2010b]. This nudging procedure has been shown to enable the model to capture the daily weather and isotopic variability well [*Risi et al.*, 2010b; *Vimeux et al.*, 2011; *Gao et al.*, 2010]. For example, in summer 2006 in average over the tropics, the daily correlation at each grid point for the large-scale vertical velocity at 500 hPa is 0.45 between the ECMWF reanalyses and the nudged simulation, compared to only 0.006 between the ECMWF reanalyses and the free-running simulation.

2.2. Data Sets and Comparison Methodology

[9] We focus on evaluating the HDO/H_2O ratio as quantified by the variable δD in ‰: $\delta D = (\frac{R}{R_{SMOW}} - 1) \cdot 1000$, where R is the HDO/H_2O ratio of the water vapor and R_{SMOW} is the Vienna Standard Mean Ocean Water (VSMOW) isotopic ratio [*Craig*, 1961]. To evaluate the simulated three-dimensional water vapor δD distribution from the surface up to the upper-troposphere, we combine various data sets that sample different parts of the atmosphere. We use several satellite data sets, which provide a global coverage: SCIAMACHY (a short-wave infra-red spectrometer) mainly sensitive to the lower troposphere, TES (a nadir-viewing thermal infrared spectrometer) which is mainly sensitive to the mid-troposphere, and ACE-FTS (an infrared solar-occultation instrument) and MIPAS (a limb infrared sounder) which are sensitive in the upper troposphere and above. In addition, we use ground-based remote-sensing (Fourier Transform Infrared) data sets derived from mid-infrared (NDACC, for which water isotopologue retrievals are performed in the framework of the project MUSICA) or near-infrared (TCCON) solar absorption spectra, and in situ measurements made at the surface and by aircraft. These data sets are listed in Table 1 and described in detail in section 3 of P1. Here we use observations made at lower latitudes (45°N–45°S).

[10] The different data sets show significant differences in their absolute δD values, meridional gradients and seasonal amplitudes (section 4.1 of P1), due to the effects of spatio-temporal sampling, instrument sensitivity and measurement errors (section 4.2 of P1). Since remote-sensing data has limited calibration and validation, we will focus the analysis on spatial and temporal variations. It is possible that those variations themselves may be in error, but the use of multiple data sets helps ensure that we draw only conclusions that are robustly supported.

[11] We follow a model-to-satellite approach to estimate what the instruments would observe if operated in the model. First, to take into account the spatiotemporal sampling of the data, we collocate the model output with the data at the daily scale. Second, to take into account the sensitivities of the different remote-sensing instruments to the true state, we apply averaging kernels to model output. Averaging kernels define the sensitivity of the retrieval at each level to the true state at each level. In P1, the model-data comparison methodology for each data set is extensively explained (section 3, Appendix C) and sources of model-data differences are quantified (section 5.1). We will focus the analysis on signals that are larger than these potential

Table 1. The Different Data Sets of Water Vapor Isotopic Composition Used for Model-Data Comparison[a]

Data Set or Network	Reference	Level	Spatial Coverage or Location; Footprint	Period	Precision	Comparison Methodology
			Satellite Measurement			
SCIAMACHY	*Frankenberg et al.* [2009]	total column, mainly sensitive in the boundary layer	global; footprint 120 × 20 km	2003–2005	40‰–100‰, reduced by averaging	collocation
TES	*Worden et al.* [2007]	600 hPa	global; footprint 5.3 × 8.5 km	2004–2008	about 40‰, reduced by averaging	collocation, application of kernels
ACE	*Nassar et al.* [2007]	down to 500 hPa	global, but small number of measurements; limb measurement	2003–2008	about 50‰, reduced by averaging	collocation, smoothing
MIPAS	*Steinwagner et al.* [2010]	down to 300 hPa	global; limb measurement	September 2002–March 2004	about 50‰, reduced by averaging	collocation, application of kernels
			Ground-Based Remote-Sensing			
TCCON network	*Wunch et al.* [2010]	total column	8 stations: Lauder, Wollongong, Darwin, Park Falls, Pasadena, Lamont, Bremen and Ny Alesund	between 1.5 and 6 years	between 5 and 35‰	collocation, application of kernels
NDACC network	*Schneider et al.* [2010]	total column and profiles up to 10 km	8 stations: Arrival Heights, Lauder, Wollongong, Izaña, Jungfraujoch, Karlsruhe, Kiruna and Eureka	between 0.5 and 13 years	5‰ for total column and 10–25‰ for profiles	collocation, application of kernels
			Ground-Based in Situ			
GNIP-vapor network of monthly samples	IAEA web site	surface	3 stations: Vienna, Ankara, Manaus	between 2 and 13 years	undocumented	collocation
Isolated data sets of daily samples	*Angert et al.* [2008]; *Risi et al.* [2010b]	surface	2 stations: Rehovot and Saclay	daily samples during 1 to 2 years	1‰	collocation
Picarro in Hawaii	*Johnson et al.* [2011]	surface at 680 hPa	Hawaii	3 weeks	5 to 10‰	collocation
Southern Ocean surface samples	*Uemura et al.* [2008]	surface	Southern Ocean	1 month	1‰	collocation
			Aircraft			
Flights in the 60s	*Ehhalt et al.* [2005]	profiles between 1.5 km and 9.2 km	3 sites in the United States: Nebraska, Santa Barbara and the Death Valley	a few isolated days	1‰	collocation
CR-AVE and TC4 campaigns	*Sayres et al.* [2010]	profiles between 475 hPa and 64 hPa	near Costa-Rica	1 week in winter 2006, 10 days in summer 2007	17‰ for ICOS and 50‰ for Hoxotope	collocation

[a]We detail the levels at which the measurements are performed or are the most sensitive, the location for ground-based data sets, the footprint for satellite data sets, the period over which we use the measurements, the precision specified in the reference papers or calculated in Appendix B of P1, and the methodology that we use for model-data comparison.

source of errors (i.e. larger than 10 or 20‰) and that are robust across data sets.

2.3. SWING2 Models

[12] We compare seven simulations by six other GCMs participating in the SWING2 inter-comparison project (http://people.su.se/∼cstur/SWING2/). Some of them are nudged by reanalyses, some of them are not (i.e. they are free-running) (Table 2). The LMDZ control simulations is one of the SWING2 simulations and has been rigorously compared with each data set through collocation with the data (see P1). Since daily values are not available in the SWING2 archive, it is not possible to collocate other model outputs with the data. Therefore, we use the LMDZ control

Table 2. List of the Different SWING2 Models Used in This Study and Their Respective Simulations[a]

GCM	Reference	Simulations	Horizontal Resolution	λ	Isotopic Processes During Rainfall
GISS	*Schmidt et al.* [2007]	free-running and nudged by NCEP	46 × 72	0.004	*Hoffmann et al.* [1998]
ECHAM4	*Hoffmann et al.* [1998]	nudged by ECMWF	64 × 128	0.003	*Hoffmann et al.* [1998]
LMDZ4	*Risi et al.* [2010b]	free-running and nudged by ECMWF	72 × 96	0.004	*Bony et al.* [2008], *Stewart* [1975] with $h_{eff} = \phi + (1 - \phi) \cdot h$ and $\phi = 0.9$
GSM	*Yoshimura et al.* [2008]	nudged by NCEP	73 × 144	0.003	*Hoffmann et al.* [1998], *Stewart* [1975] with $h_{eff} = \min(1.4 \cdot h, 1)$
CAM2	*Lee et al.* [2007]	free-running	64 × 128	0.004	*Lee and Fung* [2008], *Stewart* [1975] with $h_{eff} = \min(h + 0.5, 1)$
HadAM	*Tindall et al.* [2009]	free-running	73 × 96	0.005	*Hoffmann et al.* [1998], *Stewart* [1975] with $h_{eff} = \phi + (1 - \phi) \cdot h$ and $\phi = 0.7$
MIROC	*Kurita et al.* [2011]	free-running	73 × 96	0.003	*Hoffmann et al.* [1998], *Stewart* [1975]

[a]"Free-running" refers to standard AMIP-style simulations [*Gates*, 1992] forced by observed sea surface temperatures, and whose winds are not nudged. The λ parameter refers to the formulation of supersaturation S_i with respect to ice as a function of temperature T following $S_i = 1 - \lambda \cdot T$, involved in the kinetic fractionation during ice condensation [*Jouzel and Merlivat*, 1984]. The representation of isotopic processes during rainfall for each model is described in the indicated reference, and the calculation of the effective relative humidity around raindrops (h_{eff}) as a function of the relative humidity simulated by the physical package (h) is also given when available in references.

simulation as a reference against which we compare the SWING2 models' monthly outputs.

3. Theoretical Framework to Understand Processes Controlling Humidity and Isotopic Composition

[13] We develop a simple single-column theoretical framework to understand the sensitivity tests with the LMDZ GCM. Given its simplicity, we aim to provide qualitative insights into the main effects on humidity and water vapor isotopic composition of the different micro-physical and macro-physical processes tested in the experiments, rather than to make quantitative predictions.

3.1. Principle

[14] The theoretical framework components and notations are illustrated in Figure 2a. It is inspired by the last saturation theory as explained by *Sherwood* [1996]. *Sherwood* [1996] sets RH to a given value near saturation in convective regions, leading to a fixed profile of specific humidity (q) in convective regions. Specific humidity is then conserved in the air masses that leave the convective regions and slowly subside, leading to a decrease in RH. This framework is also consistent with the simple single-column model of *Folkins and Martin* [2005] in which the tropical mid and upper troposphere is moistened by convective clouds detrainment and dried by radiative subsidence outside the clouds. Here we extend these previous frameworks in two ways. First, we calculate the water vapor isotopic composition in addition to the humidity. Second, we take into account additional processes that are crucial for the water budget of GCMs, such as cloud microphysics, water vapor transport at the large-scale and the associated diffusion.

[15] In the real world in convective regions, ascent is concentrated in convective cores and cloud-free regions are subsident [*Emanuel et al.*, 1994], and this was the basis for frameworks such as that of *Folkins and Martin* [2005]. In GCMs however, water vapor transport by large-scale ascent is resolved by the large-scale advection scheme. The large-scale upward transport of water vapor is partly compensated (and sometimes over-compensated) by the compensating subsidence in the convection scheme [*Arakawa and Shubert*, 1974]. The proportion of the total upward water vapor transport that is treated by the large-scale advection scheme or by the convection scheme are somewhat arbitrary and model-dependent, but it impacts the vertical distribution of chemical tracers [*Lawrence and Salzmann*, 2008]. We thus expect an impact on the isotopic composition as well. Contrary to *Sherwood* [1996] and *Folkins and Martin* [2005], our goal is to interpret biases in GCMs, and therefore we need to take into account the vertical water vapor transport by the large-scale advection.

[16] To illustrate the water budget in the LMDZ GCM, we consider two regions based on monthly mean large-scale

Figure 2. (a) Illustration of the simple single-column model developed to interpret the sensitivity experiments. Characteristic profiles of specific humidity and isotopic composition $q_{t,\,dtr}$ and δD_{dtr} in convective plumes are assumed and depend on the precipitation efficiency ϵ_p in convective clouds and on the humidity and isotopic composition at the lifting condensation level q_{s0} and δD_0. The humidity and δD in the convective region, q_{asc} and δD_{conv}, are controlled by the balance between moistening by convective detrainment of air from convective plumes, moistening by large-scale ascent, and drying by large-scale condensation in anvils and cirrus clouds. In subsidence regions, the humidity and isotopic composition q_{subs} and δD_{subs} are controlled by the balance between moistening by horizontal mixing with convective regions and drying by large-scale subsidence. Vertical diffusion has also a moistening effect in both regions. (b) Major tendencies involved in the water budget of the troposphere in convective regions ($\omega_{500} < -35$ hPa/d), as diagnosed from the control simulation of LMDZ: vertical transport, convective detrainment, large-scale condensation and the residual from these 3 terms. (c) Same as Figure 2b but for subsidence regions ($\omega_{500} > 35$ hPa/d): vertical transport, large-scale condensation, horizontal advection and the residual from these 3 terms. The "vertical transport" tendency includes both the effect of large-scale vertical advection and compensating subsidence in the convective scheme. (d and e) Same as Figures 2b and 2c but as computed from the simple single-column model. The diffusive term was included as part of the vertical transport term, since in LMDZ it is intrinsic to the advection scheme.

vertical velocity at 500 hPa (ω_{500}) [*Bony et al.*, 2004]. Figure 2b shows the major tendencies involved in the water budget as simulated by the control simulation of LMDZ in regions of large-scale ascent ($\omega_{500} < -35$ hPa/day, i.e. convective regions). We combine the tendencies by large-scale vertical advection and by compensating subsidence in the convective scheme into one single tendency representing the total vertical transport in the environment (i.e. outside convective cores). To first order, in the boundary layer of convective regions, moistening by surface evaporation balances drying by downward vertical transport. In the mid and upper troposphere (between 600 hPa and 200h Pa) of convective regions, the air is moistened by convective detrainment (consistent with *Sherwood* [1996] and *Folkins and Martin* [2005] and by upward vertical transport in the environment. This moistening is balanced by drying by large-scale condensation, which represents condensation in anvils or cirrus clouds associated with convection. In the mid and upper troposphere of regions of large-scale descent ($\omega_{500} > 35$ hPa/day), the air is moistened mainly by horizontal advection from convective regions, and dehydrated mainly by downward vertical transport (Figure 2c). We

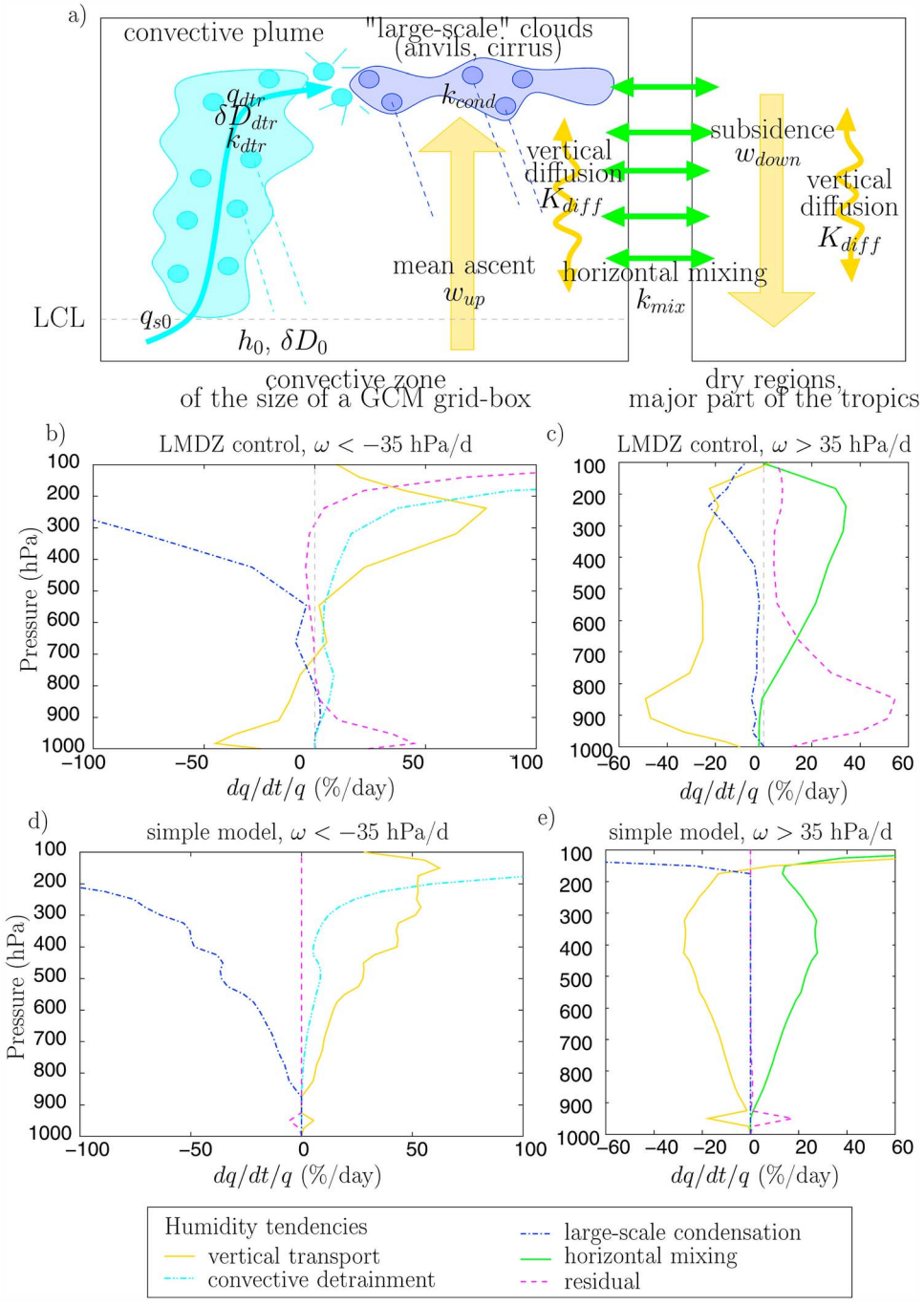

Figure 2

develop a theoretical framework that focuses on the mid and upper troposphere and represents these major tendencies in convective and subsidence regions.

3.2. Water Budget in Convective Regions

[17] In the simple framework, we assume that the temporal evolution of q in regions of large-scale ascent (q_{asc}) is driven by four contributions: (1) convective detrainment, (2) total vertical transport in the environment, (3) diffusion associated with this transport due to intrinsic numerical diffusivity of advection schemes, and (4) large-scale condensation:

$$\frac{dq_{asc}}{dt} = \left(\frac{dq_{asc}}{dt}\right)_{dtr} + \left(\frac{dq_{asc}}{dt}\right)_{env} + \left(\frac{dq_{asc}}{dt}\right)_{diff} + \left(\frac{dq_{asc}}{dt}\right)_{cond} \quad (1)$$

where we express the tendency due to convective detrainment as:

$$\left(\frac{dq_{asc}}{dt}\right)_{dtr} = k_{dtr} \cdot \left(q_{t,dtr} - q_{asc}\right) \quad (2)$$

where k_{dtr} is the rate constant of convective detrainment and $q_{t,dtr}$ is the total cloud water (vapor plus condensate) that is detraining from convective plumes. $q_{t,dtr}$ equals the humidity entrained into the plume minus the precipitation:

$$q_{t,dtr} = q_{s0} - \epsilon_p \cdot (q_{s0} - q_s) \quad (3)$$

where q_s is the humidity at saturation, q_{s0} is the specific humidity entrained into the plume and ϵ_p is the precipitation efficiency in convective updrafts. We neglect the effect of entrainment on $q_{t,dtr}$, as justified by the fact that humidity and isotopic properties of the air detrained from convective plumes is very similar to those in the adiabatic updraft, consistent with the relatively small entrainment in the Emanuel scheme [*Derbyshire et al.*, 2004; *Grandpeix et al.*, 2004]. Therefore, we assume that q_{s0} is the humidity at the lifting condensation level (LCL).

[18] We express the tendency due to vertical transport in the environment as:

$$\left(\frac{dq_{asc}}{dt}\right)_{env} = -w_{env} \cdot \frac{dq_{asc}}{dz} \quad (4)$$

where w_{env} is the vertical wind speed (positive upward) that sums the large-scale ascending speed and the downward compensating subsidence in the convective scheme. In regions of large-scale ascent, w_{env} is always positive.

[19] We express the tendency due to diffusion as:

$$\left(\frac{dq_{asc}}{dt}\right)_{diff} = K_{diff} \cdot \frac{d^2 q_{asc}}{dz^2} \quad (5)$$

where K_{diff} is the diffusivity constant associated with vertical water vapor transport.

[20] For the tendency due to large-scale condensation, as is the case in most GCMs, we assume that RH varies at the sub-grid-scale so that condensation starts for a grid average q_{asc} lower than the saturation specific humidity (q_s). As an example, we assume a uniform distribution of RH with a standard deviation σ_h. We thus get:

$$\left(\frac{dq_{asc}}{dt}\right)_{cond} = -k_{cond} \cdot (q_{asc} - q_s \cdot (1 - \sigma_h)) \quad (6)$$

where k_{cond} is the rate constant of large-scale condensation.

[21] We substitute equations (2), (4), (5), and (6) into equation (1) and solve it numerically as detailed in section 3.5. At steady state, q_{asc} is given by:

$$q_{asc} = \frac{1}{k_{dtr} + k_{cond}} \cdot \left(k_{dtr} \cdot q_{t,dtr} + k_{cond} \cdot q_s \cdot (1 - \sigma_h) - w_{env} \cdot \frac{dq_{asc}}{dz} + K_{diff} \cdot \frac{d^2 q_{asc}}{dz^2}\right). \quad (7)$$

[22] If the detrainment term dominates, then q_{asc} tends toward $q_{t,\ dtr}$. If the condensation term dominates, then q_{asc} tends toward $q_s \cdot (1 - \sigma_h)$, which is smaller. In practice, q_{asc} is bounded between these two extremes, and for reasonable sets of parameters it stays below saturation. q_{asc} increases with ϵ_p, w_{adv} and K_{diff}, and decreases with σ_h.

3.3. Water Budget in Subsidence Regions

[23] We assume that the temporal evolution of q in subsidence regions (q_{subs}) is driven by 4 contributions: (1) horizontal transport from convective regions, (2) downward vertical transport in the environment, (3) diffusion associated with this transport due to intrinsic numerical diffusivity of advection schemes, and (4) large-scale condensation:

$$\frac{dq_{subs}}{dt} = \left(\frac{dq_{subs}}{dt}\right)_{mix} + \left(\frac{dq_{subs}}{dt}\right)_{subs} + \left(\frac{dq_{subs}}{dt}\right)_{diff} + \left(\frac{dq_{subs}}{dt}\right)_{cond} \quad (8)$$

where we express the tendency due to horizontal transport from convective region as:

$$\left(\frac{dq_{subs}}{dt}\right)_{dtr} = k_{mix} \cdot (q_{asc} - q_{subs}) \quad (9)$$

with k_{mix} the rate constant of horizontal mixing. We express the tendency due to downward vertical transport as:

$$\left(\frac{dq_{subs}}{dt}\right)_{subs} = w_{subs} \cdot \frac{dq_{subs}}{dz} \quad (10)$$

where w_{subs} is the vertical wind speed (positive downward) corresponding to the large-scale subsidence. We express the two remaining tendencies in exactly the same way as for convective regions (equations (5) and (6)). We solve equation (8) numerically (section 3.5). In practice, the condensation term is very small due to the dryness of subsidence regions. This term is present only for numerical stability reasons near 100 hPa. Therefore, at steady state, q_{subs} is given approximately by:

$$q_{subs} = q_{asc} + \frac{1}{k_{mix}} \cdot \left(w_{subs} \cdot \frac{dq_{subs}}{dz} + K_{diff} \cdot \frac{d^2 q_{subs}}{dz^2}\right). \quad (11)$$

[24] It follows that all factors controlling q_{asc} also impact q_{subs}. If the mixing term dominates, then q_{subs} tends toward q_{asc}. If the subsidence term dominates, then q_{subs} reflects the value of q_{asc} much higher in altitude. In practice, q_{subs} is bounded between q_{asc} at the same level and q_{asc} higher in altitude. In addition to factors controlling q_{asc}, q_{subs} also increases with k_{mix} and K_{diff}, and decreases with w_{subs}.

3.4. Isotopic Composition

[25] Water vapor isotopic species are treated exactly like normal water during advection, mixing and diffusion, and are assumed to follow Rayleigh distillation during large-scale condensation.

[26] The isotopic ratio in convective plumes is constrained by the mass conservation underlying equation (3):

$$R_0 = f \cdot R_v + (1-f) \cdot R_c \tag{12}$$

where $f = \frac{q_s}{q_{s0}}$ is the fraction of vapor that remains after condensation in the cloud, and R_0, R_v and R_c are respectively the isotope ratio of the vapor at the LCL, the residual vapor and the accumulated condensate. We assume that R_v follows a Rayleigh distillation: $R_v = R_{v0} \cdot f^{\alpha-1}$, where α is the effective fractionation coefficient taking into account both equilibrium and kinetic fractionation consistently with LMDZ simulations [*Merlivat and Nief*, 1967; *Majoube*, 1971a, 1971b; *Jouzel and Merlivat*, 1984]. As a fraction ϵ_p of the condensate precipitates, we obtain the isotope ratio of the total water in convective plumes [*Bony et al.*, 2008]:

$$R_{dtr} = R_0 \cdot \frac{1-\epsilon_p \cdot (1-f^{\alpha})}{1-\epsilon_p \cdot (1-f)}. \tag{13}$$

[27] If the water balance in convective regions is mainly between large-scale advection and condensation, then R_{conv} is predicted by a Rayleigh distillation. In contrast, if the detrainment term dominates, the isotopic ratio R_{conv} tends toward R_{dtr}, which is much higher than predicted by a Rayleigh distillation. This is consistent with the effect of convective detrainment on upper tropospheric δD evidenced by observational studies [e.g., *Webster and Heymsfield*, 2003; *Sayres et al.*, 2010]. In practice, R_{conv} is bounded by these two extreme values. In subsidence regions, the isotopic ratio R_{subs} at a given level will be intermediate between R_{conv} at this level and R_{conv} higher in altitude. In addition, R_{subs} increases with vertical diffusion.

3.5. Numerical Application

[28] Equations (1) and (8) and their isotopic counterparts are discretized on the LMDZ vertical grid and solved numerically. We use the annual mean, tropical average temperature profile simulated by LMDZ to calculate profiles of q_s and α that will be used in all calculations. This is justified by the fact that temperature is relatively uniform in the horizontal in the tropics [*Sobel and Bretherton*, 2000] and are very similar in all our simulations. We assume that in the sub-cloud layer (below the LCL calculated at 925 hPa) RH and δD are constant at 80% and -70‰ respectively, consistent with the annual mean, tropical-average values simulated by LMDZ. These values are kept constant as a boundary condition throughout the numerical resolution, and this allows us to implicitly account for the effect of surface evaporation. The values of q and δD are also relaxed to the value predicted by a Rayleigh distillation above 100 hPa, where almost no convection penetrates. The choice of the upper bound has very little impact. The vertical profile of ϵ_p is exactly the same as in LMDZ: in the control simulation, $\epsilon_p = 0$ up to 150 hPa above LCL, $\epsilon_p = 0.99$ above 500 hPa above LCL, and ϵ_p varies linearly between these two values from 150 hPa to 500 hPa above LCL [*Emanuel and Zivkovic-Rothman*, 1999; *Bony and Emanuel*, 2001]. The vertical profile of σ_h is taken to mimic the behavior of large-scale condensation scheme of LMDZ: σ_h varies linearly from 0 at the surface to 0.4 at 100 hPa.

[29] All other variables were optimized to reproduce the tendencies simulated by LMDZ (Figures 2b and 2c) in the mid and upper troposphere. We calculate w_{up} and w_{down} by assuming that the profiles of vertical velocity in hPa/day follow a cubic shape with a maximum at 500 hPa. We take $\omega_{up} = 40$ hPa/day and $\omega_{down} = 40$ hPa/day at 500 hPa. We assume that the profile of k_{dtr} follows a Gaussian shape with a maximum at 120 hPa, a standard deviation at 300 hPa and a maximum of 0.2 day^{-1}. We assume that k_{cond} equals 0.33 day^{-1}. We assume that k_{mix} varies linearly between 0.05 day^{-1} and 1 day^{-1} from 800 hPa to 100 hPa. Finally, K_{diff} is taken so that the diffusion is equivalent to exchanging a thickness $\omega_{diff} \cdot dt$ of air between each adjacent level at each time step dt, with $\omega_{diff} = 20$ hPa/day. This value was taken as the minimum value to allow numerical stability of the single-column model.

[30] With this set of parameters, the simple single-column model reproduces satisfactorily the vertical profiles of the main tendencies involved in the mid and upper tropospheric water balance simulated by LMDZ, though in a simplified way (Figures 2d and 2e). The model fails near the surface, which is neither surprising nor problematic since we focus on mid and upper tropospheric processes. As the model was tuned to reproduce the humidity tendencies for the control simulation, the capacity of the simple framework to predict the RH and isotopic profiles simulated by LMDZ in the different sensitivity tests can be viewed as an independent check of the simple framework.

4. Sensitivity of RH to the Model Physics, Nudging and Resolution

4.1. Sensitivity to Parameterized Processes

[31] Numerous studies have shown that GCMs suffer from a moist bias compared to various data sets in the tropical upper troposphere and in the subtropical mid-to-upper troposphere, following a horse-shoe pattern [*Soden and Bretherton*, 1994; *Salathe and Chester*, 1995; *Chen et al.*, 1996; *Roca et al.*, 1997; *Chen et al.*, 1998; *Allan et al.*, 2003; *Brogniez et al.*, 2005; *Pierce et al.*, 2006; *John and Soden*, 2007; *Sherwood et al.*, 2010; *Chung et al.*, 2011]. As an illustrative example, Figure 3 compares the simulated RH in the control LMDZ simulation with the AIRS (Atmospheric Infra-Red Sounder data) data [*Aumann et al.*, 2003]. Consistent with previous studies and other GCMs, LMDZ exhibits a moist bias throughout the mid and upper troposphere in tropical average (Figure 3a). Figure 3b shows composites of RH at 350 hPa as a function of monthly mean ω_{500}. Due to a clear-sky sampling bias in AIRS [*Fetzer et al.*, 2006], upper-tropospheric RH in deep convective tropical regions could be underestimated by as much as 10–20% [*Pierce et al.*, 2006]. The moist bias seems to be stronger in regions of large-scale ascent than in regions of large-scale descent in Figure 3b, but this is likely an artifact of the clear-sky bias. This does not contradict the fact that in most GCMs, including LMDZ, the moist bias is most pronounced

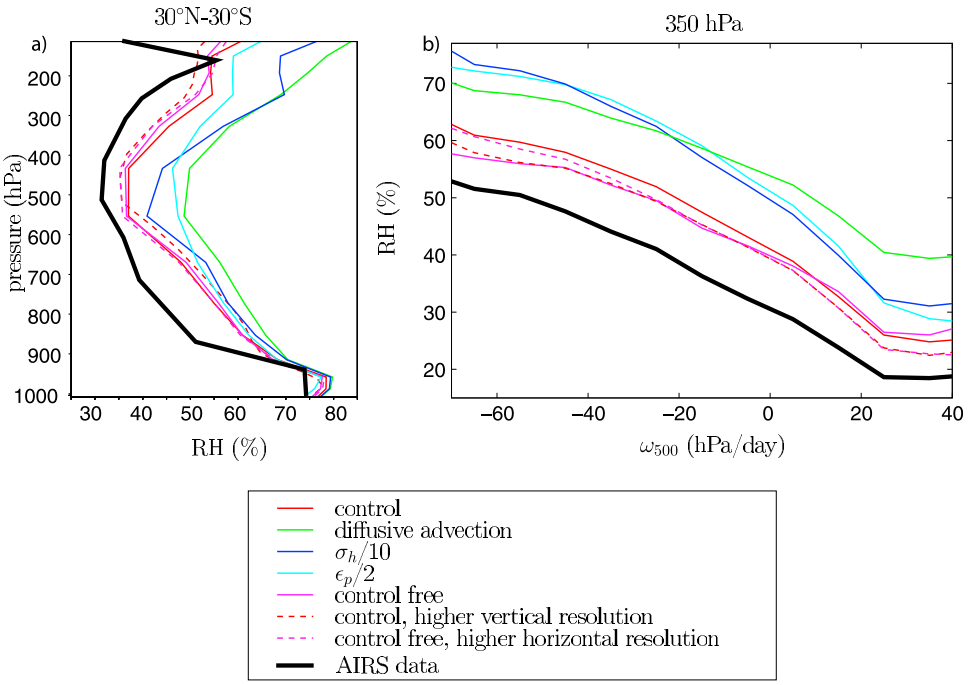

Figure 3. (a) Annual mean relative humidity (RH) profiles averaged over the tropics (30°S–30°N) simulated by the various versions of LMDZ (colors) and observed by AIRS (black). (b) Composites of monthly mean RH at 350 hPa as a function of the large-scale vertical velocity at 500 hPa (ω_{500}) over the tropics simulated by the various versions of LMDZ and observed by AIRS.

in subtropical regions. An accurate comparison of LMDZ with AIRS is beyond the scope of this paper.

[32] To understand the cause of the moist bias, we performed sensitivity tests in which the model physics was degraded in 3 different ways, corresponding to 3 possible causes for a larger moist bias (Table 3). Hereafter, they are referred to as "moist bias" simulations. We conducted tests with a larger rather than smaller moist bias because (1) the goal is to see how isotopic measurements can help understand biases, and (2) since the control simulation is already slightly biased, trying to improve the RH for different causes would lead to error compensations that would make the presentation of the results less straightforward. All these sensitivity tests are nudged by the ECMWF winds, so that the large-scale circulation is similar in all the simulations. This methodology excludes dynamical feedbacks, and thus allows us to focus on differences that are due to physical processes only.

[33] In the "diffusive advection" simulation, we replace *Van Leer*'s [1977] second-order advection scheme by a simple upstream scheme [*Godunov*, 1959]. This is the version described by *Risi et al.* [2010b] and provided to the SWING2 archive. The upstream scheme is intrinsically more diffusive. This leads to a 15% stronger moist bias throughout the tropical troposphere (Figure 3a, green). Additional tests show that most of the moistening in this simulation is due to excessive diffusion in the vertical, rather than the horizontal, advective scheme. In the theoretical framework, this simulation corresponds to an increase in K_{diff}. Vertical diffusion moistens the mid and upper-troposphere due to down gradient moisture flux and to the concavity of q profiles as a function of height. The moist bias is strongest in the subsidence region, because the diffusive moistening accumulates in air parcels as they subside from tropical regions (Figure 3b). In the theoretical framework, this is represented by the diffusion term being present in both convective and subsidence regions (equations (1) and (8)).

[34] In the "$\sigma_h/10$" simulation, the sub-grid-scale variability in water vapor, which is used to predict large-scale condensation in the *Bony and Emanuel* [2001] statistical cloud scheme, is divided by 10 at all levels. This reduces the proportion of air in the grid box exceeding saturation. Therefore, large-scale condensation decreases and contributes less to the dehydration of air masses, leading to a

Table 3. Summary of the Four Main Sensitivity Simulations Performed With the LMDZ GCM

Name	Description
Control	Control simulation described with the actual AR4 version of LMDZ4.
Diffusive advection	Same as control but a simple upstream scheme [*Godunov*, 1959] is used rather than the second order advection scheme [*Van Leer*, 1977; *Hourdin and Armengaud*, 1999]. This is the simulation described by *Risi et al.* [2010b] and provided to SWING2.
$\sigma_h/10$	Same as control but the sub-grid-scale variability in water vapor used to predict large-scale condensation and nebulosity is divided by 10.
$\epsilon_p/2$	Same as control but the precipitation efficiency in both the convective and large-scale precipitation schemes was divided by 2.

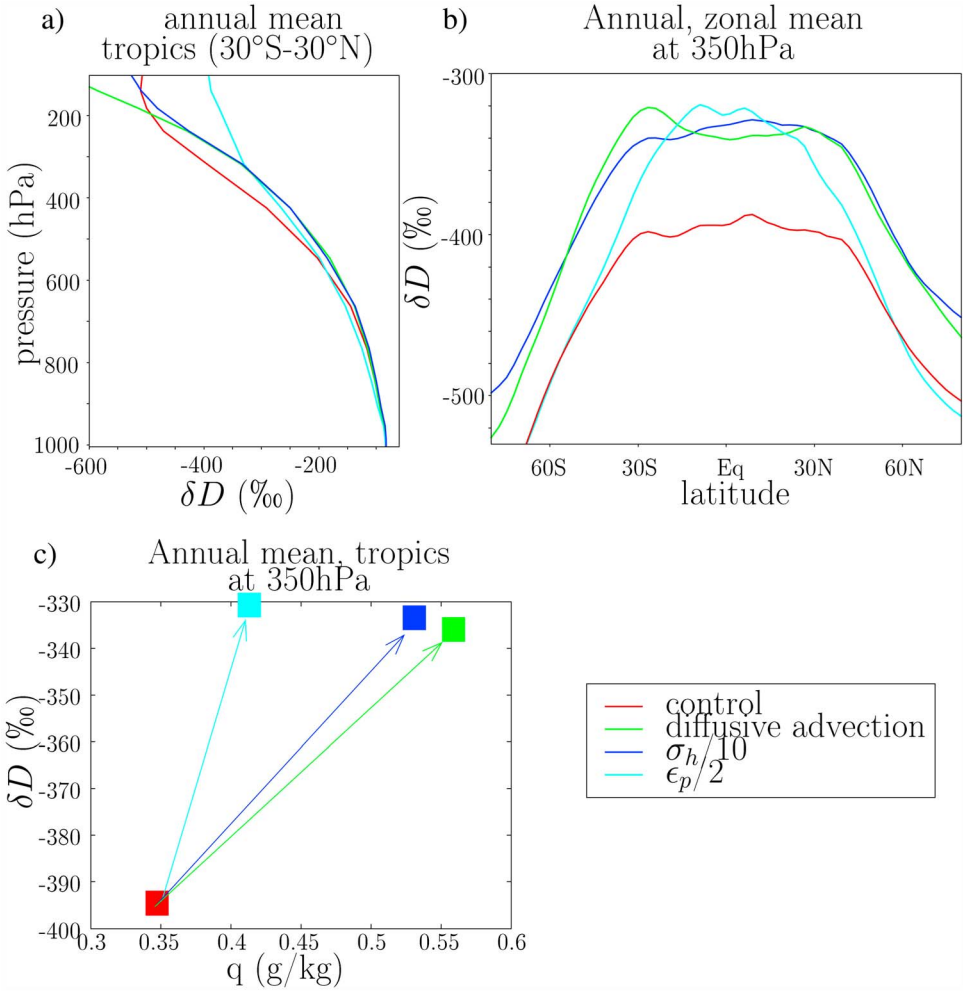

Figure 4. Comparison of annual mean water vapor δD simulated by the control simulation and by the three moist bias simulations. (a) Vertical profiles of tropical (30°S–30°N) average δD. (b) Zonal mean δD at 350 hPa. (c) Tropical average δD at 350 hPa as a function of annual mean, tropical average q at 350 hPa.

stronger moist bias by about 15% in the upper troposphere (Figure 3, blue). This is consistent with the theoretical framework, in which dividing σ_h by 10 leads to an increase in the lower bound for q_{asc} toward saturation. The effect of σ_h is largest in regions of large-scale ascent (Figure 3b), because this is where the large-scale condensation scheme plays a significant role. In subsidence regions, its effect is smaller.

[35] Finally, in the "$\epsilon_p/2$" simulation, the precipitation efficiency ϵ_p in the convective scheme was divided by 2. Therefore, a higher proportion of the condensate evaporates into the environment rather than precipitates, significantly moistening the atmosphere by 5 to 10% (Figure 3a, cyan). This is consistent with the theoretical framework, in which the increase in ϵ_p leads to an increase of $q_{t,dtr}$, which constitutes the upper bound for q_{asc}. Again, the effect is largest in regions of large-scale ascent (Figure 3b), because this is where convective detrainment plays a significant role.

[36] The large sensitivity of RH to micro- and macrophysical cloud processes seems to contradict some earlier studies. *Sherwood* [1996] argued that cloud processes act to bring the convective column close to saturation, and have thus very limited quantitative effect of RH [*Sherwood and Meyer*, 2006]. However, at the scale of a GCM grid box, the atmospheric column is not necessarily close to saturation in convective regions. Therefore, there is room for modulation of the RH by cloud processes. Then, since RH in convective regions serves as an initial condition for the RH in other dynamical regimes through large-scale transport and subsidence, RH modulations in convective regions by cloud processes propagate to other regimes. Using a simple back-trajectory model, *Dessler and Sherwood* [2000] had shown that the large-scale circulation alone could explain to first order the observed RH distribution in the upper troposphere. They showed an influence of both sub-grid-scale heterogeneity and condensate detrainment, consistent with our study, but they discarded these processes on the basis that each of them individually worsen their simulation. In GCMs however, both these processes play a simultaneous role (Figure 2b) and the degree to which they compensate each

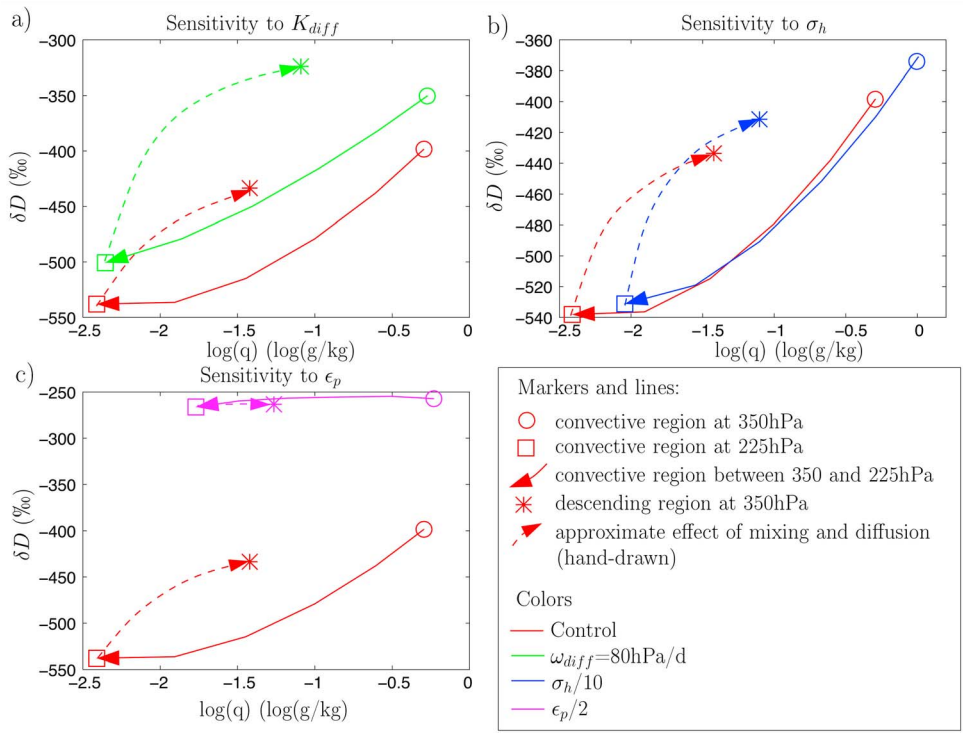

Figure 5. Illustration of how the simple theoretical model captures the behavior of q and δD for the sensitivity simulations, at 350 hPa as an example. Diagrams of δD versus $\log(q)$ are shown so that Rayleigh distillation follows approximately a straight line. On each subplot, the mechanisms for the control simulation is shown in red. The vertical profile in the convective region between 350 hPa (circle) and 225 hPa (square) follows the thick line. In subsidence regions, the humidity and δD (star) reflect a mixture between the air from convective regions at the same level and from levels above, and is further affected by vertical diffusion, following the hand-drown dashed line. These markers and lines are shown also for the three moist bias simulations: diffusive advection (Figure 5a, green), $\sigma_h/10$ (Figure 5b, blue) and $\epsilon_p/2$ (Figure 5c, pink). Note that $\log(q)$ values of -2.5, -2, -1.5, -1, -0.5 and 0 correspond to q values of 0.08, 0.14, 0.22, 0.37, 0.61 and 1 g/kg.

other affects the simulated RH. To summarize, while large-scale circulation is the major control on RH spatial variations in a given model, there is a wide margin for variations in mean RH associated with the representation of cloud processes.

4.2. Sensitivity to the Nudging and Resolution

[37] To assess the relative importance of uncertainties related to large-scale circulation in simulating RH, we compared the control simulation with nudged wind fields to a free-running simulation (i.e. without nudging). The effect on RH is however smaller (<5%) than the effect of the model physics (Figure 3, pink).

[38] Strong gradients of RH arise in the tropics and subtropics because the timescale of mixing processes is longer than that of radiative subsidence [*Pierrehumbert*, 1998; *Zhang et al.*, 2003]. A higher resolution may improve the simulation of RH by GCMs [*Sherwood et al.*, 2010]. We thus performed free-running and nudged simulations at a higher horizontal resolution (1.25° in latitude × 2.5° in longitude). The impact of resolution is slightly stronger for the free-running simulation, because it allows the model to create its own finer scale circulation. The RH is decreased by 2–3% in the subtropics, where the RH gradients are the strongest. This impact is much smaller than that of physical processes (Figure 3).

[39] Therefore, improving the representation of large-scale circulation or improving horizontal resolution has a smaller effect on the RH simulation than changing the model physics. Since the large-scale circulation is relatively well simulated in GCMs, the uncertainties that remain are related to the models physics. Therefore, while the large-scale circulation is the main control on RH, it is not the major source of uncertainty. This is confirmed by the fact that reanalyses models also exhibit the moist bias [*Salathe and Chester*, 1995; *Chen et al.*, 1998].

[40] We thus mainly focus on the sensitivity tests which are designed to test to the model physics.

[41] Coarse vertical resolution has also been suggested to contribute to the moist bias [*Pope et al.*, 2001]. We expect the vertical advection to be less diffusive at finer vertical resolution, with an effect opposite to the "diffusive advection" simulation. The simulation at higher vertical resolution (39 vertical levels rather than 19) indeed leads to a decrease in RH of about 5% (Figure 3a, dashed red). Since this simulation provides redundant information compared to the

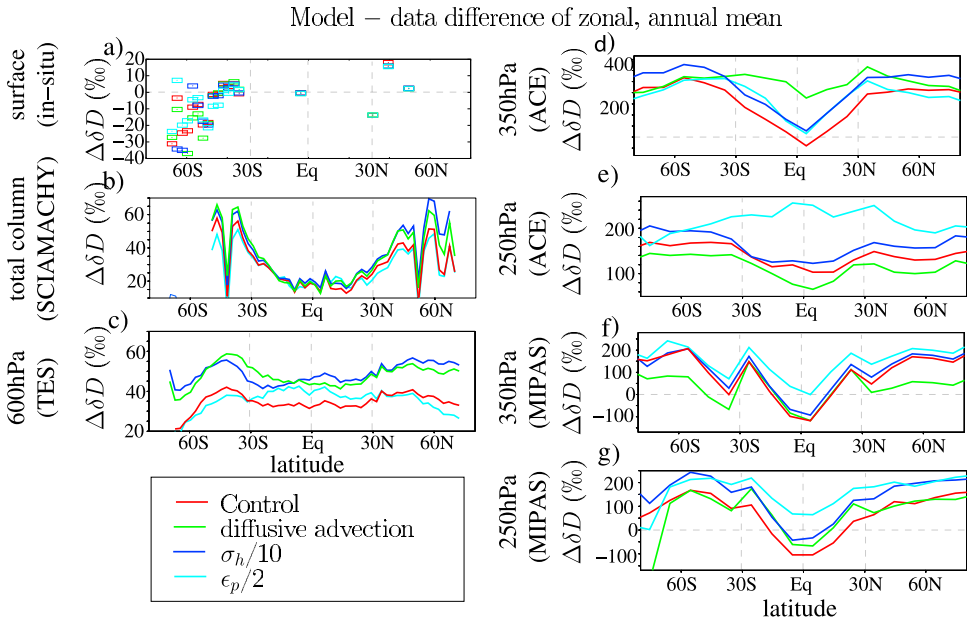

Figure 6. Model-data difference for zonal, annual mean δD at different levels and compared to different data sets: (a) at the surface compared to in situ data, (b) total column compared to SCIAMACHY, (c) at 600 hPa compared to TES, (d) at 350 hPa compared to ACE, (e) at 250 hPa compared to ACE, (f) at 350 hPa compared to MIPAS, and (g) at 250 hPa compared to MIPAS. The model-differences are shown for the control simulation and each of the three moist bias simulations. Model output was collocated and kernel-weighted as explained in section 2.2. Right column. Ground-based remote-sensing and in situ data sets are not shown in the plots for clarity, but their results are summarized in Table 4.

"diffusive advection" simulation, we focus on the latter for the sake of brevity.

5. Isotopic Fingerprint of Different Causes for the Moist Bias

[42] The goal of this section is threefold. First, we compare the isotopic behavior associated with the different causes of a moist bias in our sensitivity tests. If the isotopic behavior is significantly different between the simulations in a way that is complementary to the behavior of RH, then this isotopic behavior could be used as a diagnostic for the moist bias. Second, we interpret the isotopic behavior using the theoretical framework, to check that we understand the processes at play. Third, we compare the simulations to the data, to identify which one most closely matches the observations and to assess to what extent the isotopic measurements can help discriminate between the different simulations.

5.1. Zonal, Annual Means

[43] Figure 4a compares tropical mean profiles of δD for the control and moist bias simulations. In all moist bias simulations δD is higher than in the control between 500 and 200 hPa. The increase in δD is the strongest in "$\epsilon_p/2$" in the upper troposphere. Figure 4b compares the zonal mean δD at 350 hPa. The level 350 hPa is chosen as representative of the upper troposphere where the isotopic differences between the tests are the strongest. Most of our analysis focuses on this level. In the "advective diffusion" and "$\sigma_h/10$" simulations, upper tropospheric δD increases at all latitudes (Figure 4b), whereas in the "$\epsilon_p/2$" simulation, the δD increase is concentrated in the tropics, consistent with the convective detrainment acting mainly in the tropics. The increase in δD does not obviously relate to the increase in q or RH following Rayleigh distillation: the increase in tropical δD is largest in the "$\epsilon_p/2$" simulation, although the increase in q or RH is smallest for this simulation (Figure 4c). This shows that δD is particularly sensitive to convective detrainment and provides additional information compared to traditional humidity variables.

[44] To understand the δD increase in the moist bias simulations, in Figure 5 we illustrate the results of the theoretical framework (section 3) at 350 hPa in a δD versus log (q) diagram, in which Rayleigh distillations are approximately straight lines. The solid red arrow shows the δD profile in convective regions from 350 hPa (red circle) up to 225 hPa (red square) for the control case. In convective regions, δD decreases as q decreases with altitude, but less steeply than predicted by Rayleigh distillation, due to convective detrainment of condensate [e.g., *Moyer et al.*, 1996]. Then, as explained in section 3.3, δD in subsidence regions at 350 hPa is a mixture between δD in convective regions at 350 hPa and δD in convective regions higher up (e.g. 225 hPa). The dashed red arrow shows the effect of mixing the air at 350 hPa and 225 hPa, combined with the effect of vertical diffusion. The red star shows the resulting δD at 350 hPa in subsidence regions. Since mixing lines are curved in a way that leads to higher δD compared to Rayleigh lines [e.g., *Brown et al.*, 2008; *Galewsky and Hurley*, 2010; *Noone et al.*, 2011], δD in subsidence regions is higher for a given q than in convective regions. Vertical

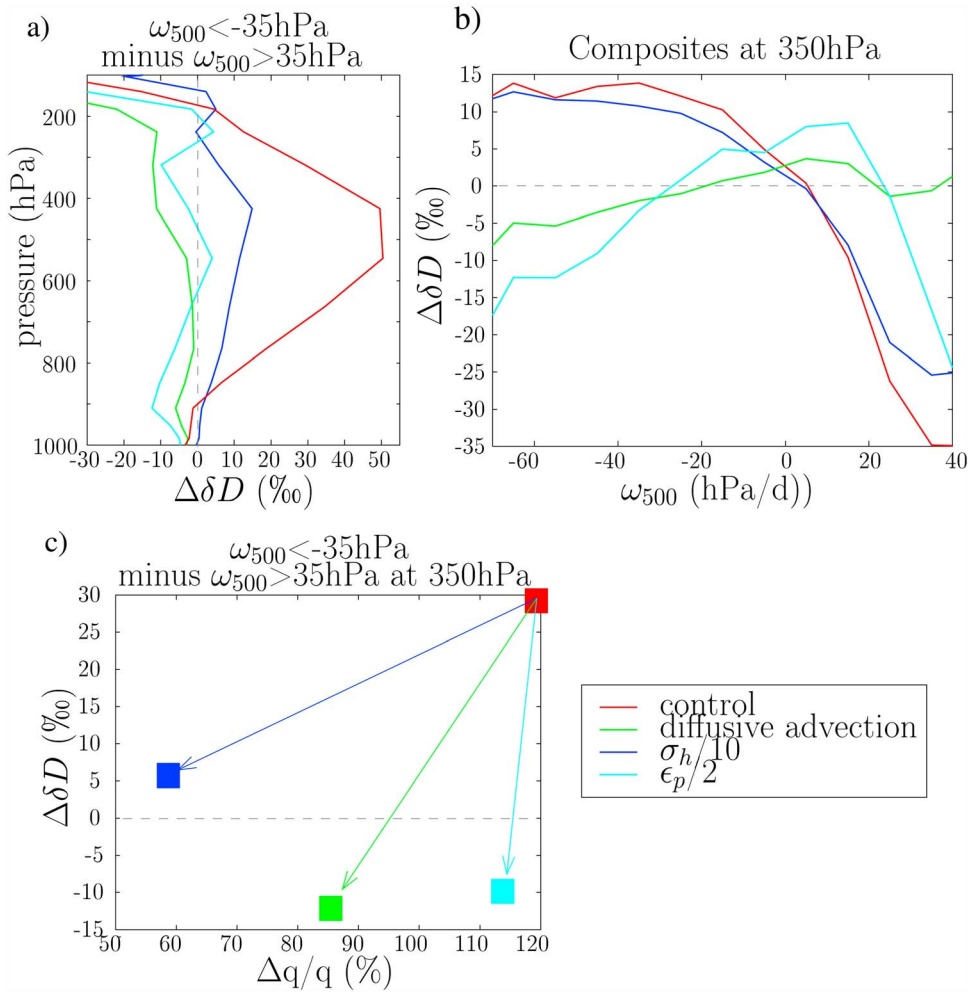

Figure 7. Comparison of water vapor δD simulated by the control simulation and the by three moist bias simulations, binned into dynamical regimes. (a) Vertical profiles of the difference between composite of monthly mean δD in regions of large-scale ascent (tropical grid cells where $\omega_{500} < -35$ hPa/d) and composite of monthly mean δD in subsidence regions (tropical grid cells where $\omega_{500} > 35$ hPa/d). The variable ω_{500} refers to the large-scale vertical velocity at 500 hPa, with negative (positive) values in regions of large-scale ascent (subsidence). (b) Composites of monthly mean δD at 350 hPa as a function of ω_{500} over the tropics. The annual mean, tropical average was subtracted to focus on contrasts between dynamical regimes. (c) Composite of monthly mean δD at 350 hPa in convective regions minus that in subsidence regions, as a function of the same difference for q. The difference in q was normalized and expressed in % as follows: $(q_{asc} - q_{subs})/(q_{asc} + q_{subs}) \cdot 200$.

diffusion also contributes to the δD increase, since diffusion acts like mixing.

[45] We now use the theoretical framework to interpret the δD difference between the sensitivity tests. When vertical diffusion is stronger (here, we take ω_{diff} = 80 hPa/d compared to 20 hPa/d in the control), convective regions are slightly moistened and have a significantly higher δD due to the curvature of mixing lines (Figure 5a, green). In subsidence regions, the δD is even further increased, due to the additional diffusion along the way. In the "$\sigma_h/10$" simulation, the distillation curve in convective regions remains approximately the same, but since large-scale condensation is less efficient, the distillation does not go as far as in the control (Figure 5b, blue). q and δD are thus higher in convective regions and this signature is conserved during the subsidence, leading to higher q and δD everywhere. In "$\epsilon_p/2$", more condensate is detrained from convective towers, so that δD in convective regions is much higher, especially in the upper troposphere where detrainment is largest (Figure 5c, cyan). This higher δD is then conserved during subsidence in subsidence regions.

[46] To summarize, the increase in δD associated with the moistening has a very different cause in each of the three sensitivity tests. As a result, for a given increase in q relatively to the control, the δD increase is very different between the tests (Figure 4c). In particular, the theoretical model is able to predict that for "$\epsilon_p/2$", δD is 3–4 times more sensitive to changes in q than for "advective diffusion" or "$\sigma_h/10$".

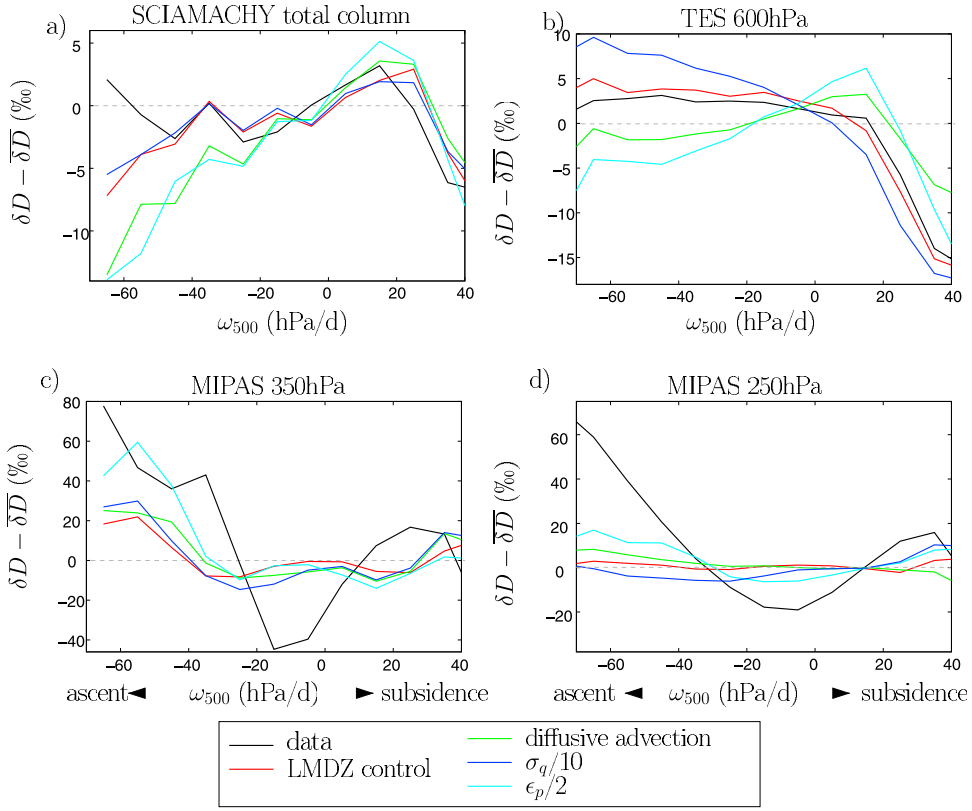

Figure 8. Composites of monthly mean δD as a function of ω_{500} for the control simulation and the three moist bias simulations compared to the data at different levels. (a) Total column δD compared to SCIAMACHY, (b) at 600 hPa compared to TES, (c) at 350 hPa compared to MIPAS, and (d) at 250 hPa compared to MIPAS. Model outputs were collocated and kernel-weighted as explained in section 2.2.

[47] Could isotopic observations help discriminate between the different simulations? Figure 6 shows the model-data differences at different levels and for different data sets. The differences between simulations evidenced previously persist even after taking into account the spatiotemporal sampling and instrument sensitivity effects: for example, "$\epsilon_p/2$" remains more enriched than all other simulations in the tropical upper troposphere by more than 100‰. However, in absence of absolute calibration for upper-tropospheric data sets, it is impossible to identify the most realistic simulation in terms of absolute δD.

5.2. Variations With Dynamical Regime

[48] In the tropics, it is convenient to examine model output as a function of dynamical regime characterized by the monthly mean large-scale vertical velocity ω_{500} [*Bony et al.*, 2004]. Figure 7a shows profiles of δD differences between tropical regions of large-scale ascent and descent, and Figure 7b shows δD at 350 hPa as a function of ω_{500}. The sensitivity tests show very different behaviors, both quantitatively and qualitatively. The only common feature between all simulations is that at the surface, convective regions have a lower δD than subsidence regions (Figure 7a). Strong precipitation events have long been observed to be associated with a lower δD in the precipitation and the surface vapor (i.e. amount effect [*Dansgaard*, 1964]), and this has been shown to involve processes restricted to the lower troposphere such as rain re-evaporation or unsaturated downdrafts [*Lawrence et al.*, 2004; *Risi et al.*, 2008, 2010a; *Field et al.*, 2010]. In contrast, from 900 to 200 hPa in the control simulation, δD is lower in regions of large-scale subsidence than in regions of large-scale ascent, by up to 50‰ around 500 hPa. This is expected from the simple model (Figure 5, stars versus circles), since the low δD values found in the upper troposphere of large-scale ascent regions are largely conserved during subsidence. The decrease of δD as ω_{500} increases is the strongest for $\omega_{500} > 0$ hPa (Figure 7b).

[49] In the "$\sigma_h/10$" simulation, the contrast between convective and subsidence regions is slightly weaker, with higher δD in subsidence regions. In the "$\epsilon_p/2$" simulation, the decrease of δD as ω_{500} increases is similar to the control for $\omega_{500} > 20$ hPa/d. However, for $\omega_{500} < 20$ hPa/d, δD decreases as ω_{500} decreases throughout the entire troposphere. Similarly, in the "diffusive advection" simulation, δD decreases as ω_{500} decreases for $\omega_{500} < 20$ hPa/d. In addition, contrary to all other simulations, δD does not decrease with ω_{500} for $\omega_{500} > 20$ hPa/d. Even in strongly subsiding regions, δD is always higher than in convective regions throughout the free troposphere.

[50] We notice that the spread in our simulations is not obviously linked to the behavior of q: "advective diffusion" exhibits the most negative δD difference between convective and subsidence regions, but not the weakest contrast for q (Figure 9). We also checked that the isotopic behavior is not related to how the precipitation rate varies with ω_{500}. This

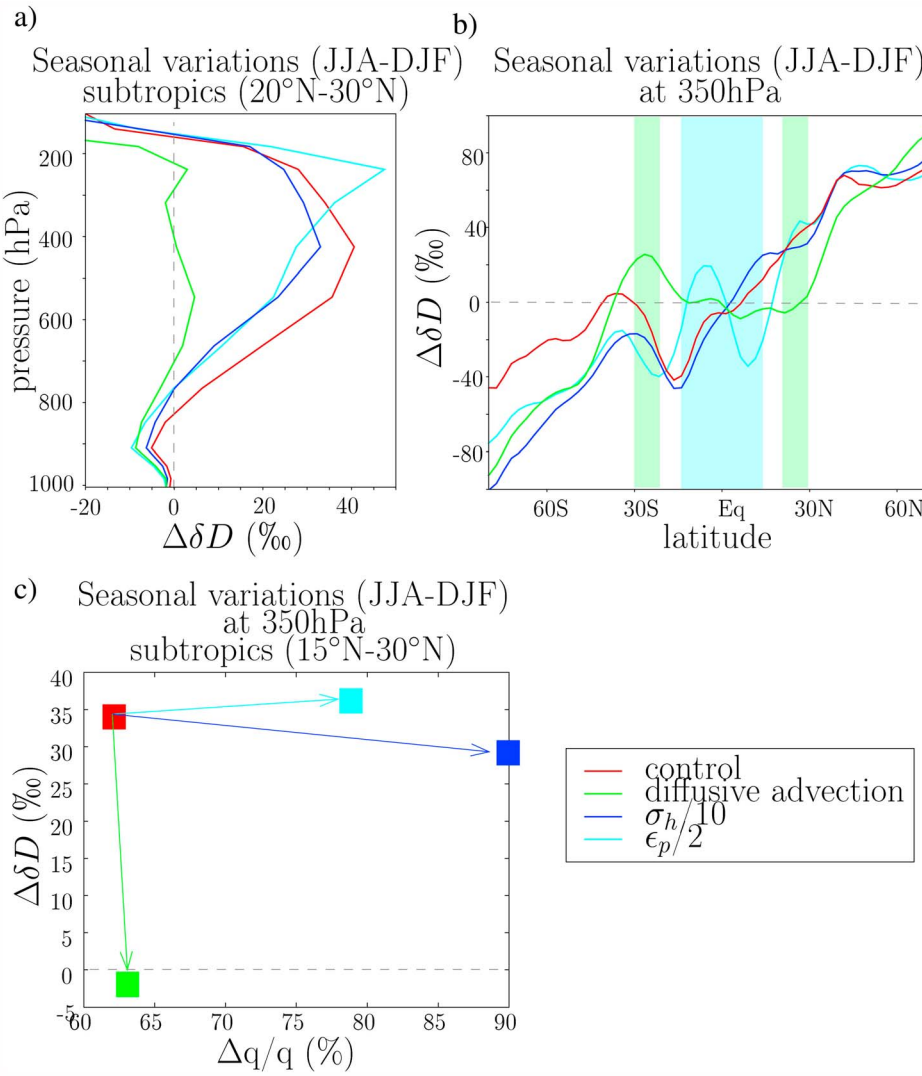

Figure 9. Comparison of seasonal variations of water vapor δD simulated by the control simulation and by the three moist bias simulations. (a) Vertical profiles of seasonal variations (JJA-DJF) in δD in average over the Northern subtropics (20°N–30°N). (b) Seasonal variations at 350hPa as a function of latitude. Cyan and green shadings highlight the deep tropical (15°S–15°N) and subtropical (20°N–30°N) regions where the seasonality is reversed in the "$\epsilon_p/2$" and "diffusive advection" simulations respectively. (c) Seasonal variations of δD at 350hPa in average over the Northern subtropics, as a function of the same seasonal variations for q. The variation in q was normalized by annual mean q and expressed in %.

shows again that δD provides complementary information on the relative magnitude of processes contributing to the moisture balance.

[51] We use the simple theoretical framework to explain the different isotopic behavior. In the "diffusive advection" simulation, the stronger vertical diffusion in subsidence regions leads to a stronger δD increase than in the control. If the diffusion is sufficiently strong, it can overcome the effect of subsidence, leading to higher δD in subsidence regions than in convective regions (Figure 5a). In the "$\sigma_h/10$" simulation, q and δD are higher at all levels in convective regions, so this signal is preserved during subsidence (Figure 5b). Hence, the δD contrast between convective and subsidence regions is similar to that in the control. Finally, in the "$\epsilon_p/2$" simulation, the vertical gradient in δD in the convective region is weaker than in the control, due to the effect of condensate detrainment in the upper troposphere (Figure 5c). Therefore, the effect of subsidence on the δD is weaker, leading to the weaker contrast between subsidence and convective regions. In addition, the very low δD in very convective regions can be due to the much weaker convective mass fluxes in the "$\epsilon_p/2$" simulation than in the control. Indeed, since most of the condensate detrains rather than precipitates, the model has to produce precipitation by an alternative means, i.e. by large-scale condensation. Therefore, in convective regions, large-scale condensation is stronger and convective detrainment fluxes are smaller in the "$\epsilon_p/2$" simulation than in the control, explaining why δD is so low in convective regions in the "$\epsilon_p/2$" simulation.

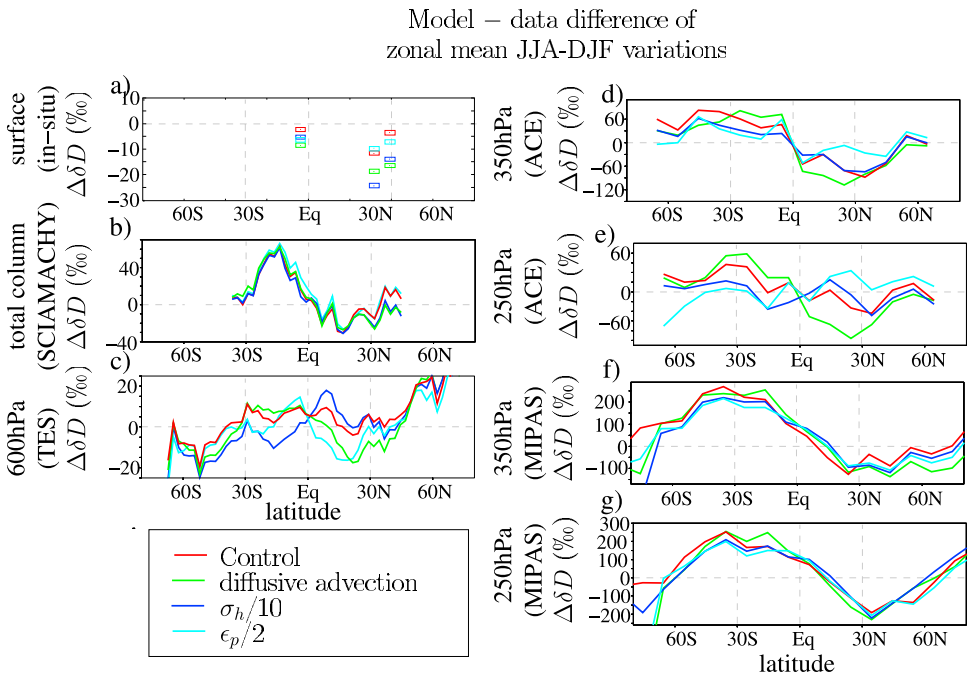

Figure 10. Same as Figure 6 but for model-data differences of zonal mean seasonal variations (JJA-DJF). Note that two kinds of differences (model-data and JJA-DJF) have been compacted into the $\Delta\delta D$ notation.

[52] Figure 8 shows that even after taking into account spatiotemporal sampling and instrument sensitivity corresponding to the different data sets, the main δD characteristics of our simulations remain. The isotopic data could thus help discriminate which of these very distinct behavior better represents the real atmosphere. In the lower and mid troposphere, the control simulation has the best agreement with SCIAMACHY and TES, whereas the "diffusive advection" and "$\epsilon_p/2$" simulations exhibit excessively low δD values in convective regions. (Figures 8a and 8b). In the upper-troposphere however, none of the simulations is able to match the strong increase in δD in regimes of large-scale ascent.

5.3. Seasonal Variations

[53] In the tropics and the subtropics, much of the seasonal variations are associated with seasonal variations in dynamical regimes. When ascending motions are more frequent, δD is expected to be higher as explained in section 5.2. In the control simulation, at all latitudes, upper tropospheric δD is higher in summer than in winter (Figures 9a and 9b). This is consistent with more frequent ascending motions in summer than in winter due to the location of the inter-tropical convergence zone. In the subtropics in both hemispheres, the higher δD in summer holds from 900 hPa to 200 hPa, so it is very robust. The maximum seasonality is around 500 hPa, as was the case for variations with ω_{500}.

[54] As was the case for variations with ω_{500}, the "$\sigma_h/10$" simulation has an isotopic behavior that is quite similar to the control. "$\epsilon_p/2$" also has a similar behavior in the subtropics (where large-scale motions are mostly subsiding), but δD is lower in summer than in winter in deep tropical regions (15°S–15°N) (Figure 9b). This is consistent with the very low δD in convective regions in this simulation (Figure 9). Finally, in the "diffusive advection" simulation, the seasonality is very weak, or even reversed, in the subtropics in both hemispheres (20°S–30°S and 20°N–30°N). This is consistent with the δD being higher in subsidence regions than in convective regions in this simulation.

[55] Therefore, the understanding of isotopic variations across dynamical regimes (section 5.2) allows us to understand the different behaviors of our simulations in terms of isotopic seasonality. Again, the different isotopic behaviors are not obviously related to those in humidity (Figure 9c), showing the added value of isotopic measurements to discriminate between the simulations.

[56] At all levels, the control simulation underestimates the isotopic seasonality in the subtropics (Figure 10). This is robust in the comparisons between the model and all data sets (in situ, ground-based remote-sensing and satellites). The robustness of this result is further discussed in P1. Therefore, the underestimated or even reversed seasonality in the "diffusive advection" simulation worsens the model-data agreement. Compared to ACE for example, the δD seasonality is more underestimated in the "diffusive advection" simulation than in the control by 40–50‰ in the Northern subtropics (Figures 10d and 10e). The magnitude of this difference is unlikely to be affected by absolute calibration problems in the data since we are looking at variations. In addition, it is larger than any additional sources of model-data comparison uncertainties detailed in P1. Therefore, the deterioration of the simulated subtropical seasonality in the "diffusive advection" simulation is robustly constrained by the comparison with the ACE data. It is also observable in the subtropics at 600hPa compared to TES (Figure 10c) and compared to MIPAS at 350 hPa (Figure 10f) and at 250 hPa (Figure 10g), except for MIPAS in the Northern Hemisphere.

[57] To measure the degree to which our simulations capture the δD seasonality in the subtropics and lower

Table 4. Quantitative Metrics to Compare the Model-Data Agreement Between the Different LMDZ Simulations[a]

Feature	Metric	Region	Data Set	Level	Control	Diffusive Advection	$\sigma_h/10$	$\epsilon_p/2$
Zonal mean seasonal variations (JJA-JF)	amplitude ratio	20°N–30°N	SCIAMACHY	total column	*0.67*	**0.40**	0.41	0.60
	amplitude ratio	20°N–30°N	TES	600 hPa	*1.02*	**0.27**	1.14	0.57
	amplitude ratio	20°N–30°N	MIPAS	350 hPa	**−0.06**	0.02	0.21	*0.26*
	amplitude ratio	20°N–30°N	ACE	350 hPa	0.37	**0.07**	*0.39*	0.38
	amplitude ratio	20°N–30°N	MIPAS	250 hPa	0.11	**−0.35**	0.11	*0.92*
	amplitude ratio	20°N–30°N	ACE	250 hPa	0.31	**−0.99**	0.88	*1.92*
	amplitude ratio	20°N–30°N	SCIAMACHY	total column	0.13	**−0.09**	*0.14*	0.02
	amplitude ratio	20°N–30°N	TES	600 hPa	0.35	**0.19**	*1.17*	1.10
	amplitude ratio	20°N–30°N	MIPAS	350 hPa	−0.21	**−0.26**	−0.10	*0.04*
	amplitude ratio	20°N–30°N	ACE	350 hPa	−0.16	**−0.39**	−0.01	*0.16*
	amplitude ratio	20°N–30°N	MIPAS	250 hPa	−0.52	**−1.05**	0.20	*0.51*
	amplitude ratio	20°N–30°N	ACE	250 hPa	−0.14	**−0.72**	0.72	*0.98*
Seasonal variations (JJA-JF) at all subtropical and stations (15°S–45°S and 15°S–45°N)	amplitude ratio	Wollongong (34.41°S)	NDACC	total column	0.72	**0.51**	0.64	*0.74*
	amplitude ratio	Wollongong (34.41°S)	TCCON	total column	0.40	**0.30**	*0.60*	0.32
	amplitude ratio	Wollongong (34.41°S)	NDACC	600 hPa	*2.72*	**1.71**	2.50	2.86
	amplitude ratio	Izaña (28.30°N)	NDACC	600 hPa	*0.37*	**0.21**	0.28	0.30
	amplitude ratio	Pasadena (34.2°N)	TCCON	total column	**−0.79**	−0.64	*0.82*	−0.84
	amplitude ratio	Oklahoma (36.6°N)	TCCON	total column	0.59	**0.35**	0.45	*1.0*
	amplitude ratio	Santa Barbara (34°N)	Ehhalt	350 hPa	0.84	**0.29**	0.80	0.85
	amplitude ratio	Death Valley (36°N)	Ehhalt	350 hPa	0.38	**0.11**	0.39	0.34
	amplitude ratio	Nebraska (41.83°N)	Ehhalt	350 hPa	0.93	**0.69**	0.83	0.89
Spatial variations of annual mean	standard deviation ratio	45°S–45°N	SCIAMACHY	total column	**0.42**	0.48	0.43	*0.59*
	standard deviation ratio	45°S–45°N	TES	600 hPa	0.85	**0.74**	0.80	*1.07*
	standard deviation ratio	45°S–45°N	MIPAS	250 hPa	**0.25**	*0.46*	0.32	0.45
	correlation	45°S–45°N	SCIAMACHY	total column	*0.62*	*0.62*	0.61	**0.59**
	correlation	45°S–45°N	TES	600 hPa	*0.93*	0.91	0.92	**0.86**
	correlation	45°S–45°N	MIPAS	250 hPa	0.54	0.61	**0.51**	*0.73*
Spatial variations of seasonal variations (JJA-JF)	standard deviation ratio	45°S–45°N	SCIAMACHY	total column	**0.31**	0.40	**0.31**	*0.46*
	standard deviation ratio	45°S–45°N	TES	600 hPa	0.96	**0.82**	*0.99*	1.18
	standard deviation ratio	45°S–45°N	MIPAS	250 hPa	**0.33**	0.36	0.37	*0.44*
	correlation	45°S–45°N	SCIAMACHY	total column	0.40	*0.45*	0.44	0.43
	correlation	45°S–45°N	TES	600 hPa	*0.73*	**0.61**	**0.61**	0.63
	correlation	45°S–45°N	MIPAS	250 hPa	0.47	**0.13**	*0.59*	0.53
Daily variability	standard deviation ratio	Izaña (28.30°N)	ground-based remote-sensing	4.2 km	*0.69*	**0.40**	0.51	0.68
	correlation	Izaña (28.30°N)	ground-based remote-sensing	4.2 km	**0.39**	*0.45*	0.42	0.34

[a]For each feature that we try to evaluate, we look at different metrics, regions, data sets and/or levels. To evaluate the seasonality, we calculate the ratio of amplitude as the amplitude of seasonal variations (JJA-DJF) for the simulation divided by that for the data, in average over the specified region or at the specified site. To evaluate spatial variations, we calculate the standard deviation ratio as the standard deviation in the simulation divided by that in the data, and the correlation between the simulation and the data. The same applies to evaluate daily variations at Izaña. For a each metric, the simulation with the lowest (resp. highest) seasonality, standard deviation or correlation is highlighted in bold (resp. in italic).

midlatitudes, we calculate the ratio of the simulated JJA-DJF variations to the observed JJA-DJF variations, at different levels, in different hemispheres and compared to different data sets (Table 4, zonal mean seasonal variations and seasonal variations (JJA-DJF)). Although there is no consensus on which simulation performs the best, the "advective diffusion" simulation has the lowest seasonality in 20 of these metrics, corresponding to the worst model-data agreement in 19 of these metrics. For example, for the average over 20°S–30°S and over 20°N–30°N, the "advective diffusion" simulation has the worst underestimate of the seasonality compared to all satellite data sets except when compared to MIPAS in the Northern Hemisphere. Between 20°S–45°S and 20°N–45°N, this is also the case for all of the aircraft data sets and at all ground-based remote-sensing stations except at Pasadena.

[58] To summarize, in LMDZ, when a moist bias is due to excessively diffusive vertical advection, the isotopic seasonality in the subtropics is distinctively lower. This can be robustly identified by comparison with almost all data sets, especially with ground-based remote-sensing and ACE data sets.

5.4. Spatial Variations

[59] Spatial variations partially reflect variations in dynamical regimes. Spatial variations in the control simulation and in the SCIAMACHY, TES and MIPAS data sets are extensively discussed in P1. To measure the degree to which simulations reproduce spatial patterns of annual mean δD, we calculate the spatial correlations between simulated and observed annual mean δD, and the ratio of the simulated spatial standard deviation to the observed spatial standard deviation of annual mean δD (Table 4, spatial variations of annual mean). To measure the degree to which simulations reproduce spatial patterns of δD seasonality, we calculate the same metrics for JJA-DJF variations (Table 4, spatial variations of seasonal variations (JJA-DJF)). No consensus emerges regarding the best or worst performing simulation. The control simulation is most frequently the best in capturing the spatial patterns (as quantified by correlations). In

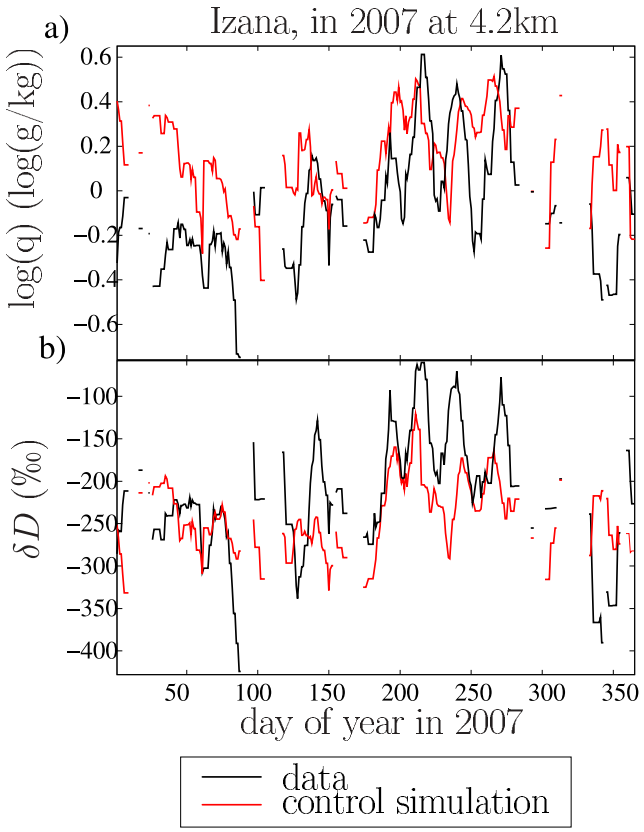

Figure 11. (a) Daily specific humidity q (in logarithmic scale) and (b) vapor δD at 4.2 km retrieved by the ground-based remote-sensing at Izaña (solid black) and simulated by the four versions of LMDZ, during the year 2007. Time series were applied a 5-day running mean, and model outputs were collocated with the data and kernel-weighted with averaging kernels. On the right are shown the average values plus and minus one standard deviation. Note that $\log(q)$ values of -0.6, -0.4, -0.2, 0, 0.2, 0.4 and 0.6 correspond to q values of and 0.25, 0.40, 0.82, 1, 1.22, 1.49 and 1.82 g/kg.

contrast, the "$\epsilon_p/2$" simulation is most frequently the best in capturing the amplitude of spatial variations (as quantified by the ratio of standard deviation), consistent with the strong δD variations with ω_{500} in the latter simulation. Overall, spatial variations of isotopic ratio are less capable at discriminating between the simulations than is the seasonality.

5.5. Intraseasonal Variability in the Subtropics

[60] We have shown that the different sensitivity tests behave differently in subsidence regions (section 5.3). In the subtropics, strong synoptic and intraseasonal variability in RH arise because of strong contrasts between highly dehydrated air and moist plumes from the tropics [*Pierrehumbert*, 1998; *Pierrehumbert and Roca*, 1998; *Zhang et al.*, 2003]. We thus look in more details at the daily ground-based remote-sensing data at the subtropical station Izaña. In the theoretical framework, Izaña can be considered a subsidence region in which the daily data capture variability in the balance of subsidence and horizontal mixing from convective regions nearby.

[61] Despite the nudging, GCMs have difficulties in capturing the timing of the subtropical synoptic and intraseasonal variations. Figure 11a shows the comparison of daily data for the year 2007 at 4.2 km, when LMDZ captures best the timing of humidity modulations. The data features very strong intraseasonal variations, with peak-to-peak variations in q of 4 g/kg and in δD of 150‰ in summer (Figures 11a and 11b). In the control simulation, the q fluctuations are slightly underestimated and the air is on average too moist (consistent with section 5.1). The magnitude of δD fluctuations is also slightly underestimated.

[62] In moist bias simulations, annual mean q and δD are higher (Figure 12, consistent with section 5.1). In the "diffusive advection" simulation, the standard deviations of fluctuations are 25% weaker for q and 45% weaker for δD than in the control. This is associated with an underestimated slope of δD vs q (Figure 11a). This is consistent with the accumulating effect of continuous vertical diffusion during subsident transport from the tropics to Izaña. q and δD thus increase most strongly during the driest periods, when air travels for a longer period. Hence the lower variability in q and δD. In addition, due to the curvature of mixing lines (Figure 5a), diffusion increases δD much more strongly for a given increase in q than predicted by Rayleigh distillation. Hence the lower slope of δD vs q.

[63] In contrast, in the "$\sigma_h/10$" and "$\epsilon_p/2$" simulations, q and δD are mainly affected in convective regions where most of the large-scale condensation and convective detrainment take place. The increases in q and δD in convective regions are preserved to some extent in subsidence regions, but the slopes of δD vs q are not as strongly affected as for the "diffusive advection" simulation (Figures 12b and 12c).

[64] Therefore, the tests exhibit different daily variations in the subtropics, and these are consistent with the predictions from the theoretical framework under different dynamical regimes. The control simulation captures best the timing and amplitude of δD variations, while the "diffusive advection" simulation underestimates δD fluctuations the worst (Table 4, daily variability). Therefore, this remote-sensing data set, combined with all the other data sets documenting isotopic seasonality, can robustly identify the shortcoming in the numerical scheme used to account for vertical transport in models. This results can be obtained from both daily and seasonal mean data.

6. Isotopic Seasonality in the Subtropics as a Diagnostic for the Moist Bias

[65] We have shown that different processes potentially explaining the moist bias commonly seen in GCMs have a different isotopic signature, in the annual mean, seasonal cycle and intraseasonal variability, as summarize in Table 5. We have also shown that this isotopic signature provides complementary information compared to humidity variables. Compared to the data, the most pronounced isotopic bias is the underestimated or reversed δD subtropical seasonality in the "diffusive advection" simulation. This can be seen at all mid and upper tropospheric levels and in most data sets (section 5.3). Therefore, we focus on using the isotopic seasonality as an observable diagnostic to understand the cause of the moist bias in GCMs. In the next section, we

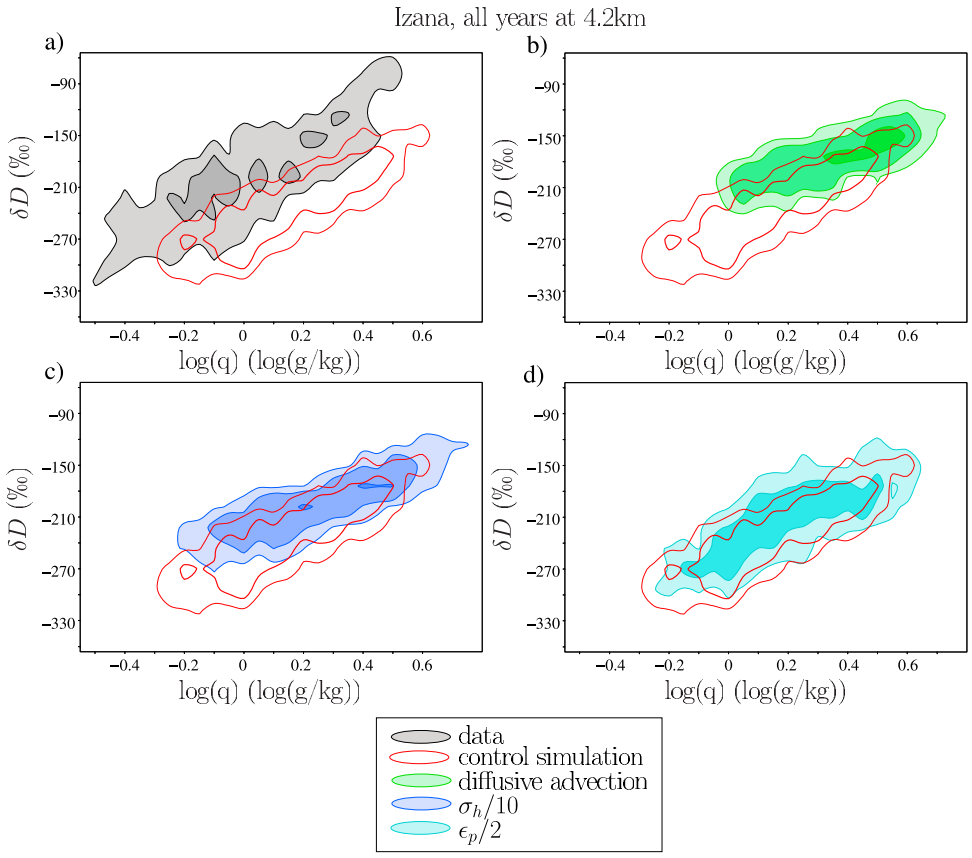

Figure 12. Probability density function (PDF) for the joint $q - \delta D$ distribution at 4.2 km at Izaña. The scale for q is logarithmic: log(q) values of −0.4, −0.2, 0, 0.2, 0.4 and 0.6 correspond to q values of and 0.40, 0.82, 1, 1.22, 1.49 and 1.82 g/kg. The PDFs were calculated from all years of data and binned into bins of 0.05 log(g/kg) and 24‰ and lines correspond to densities of 0.5% (thinnest lines or lightest colors), 1.5% (medium lines and colors) and 4% (thickest lines and darkest colors). For clarity, the PDF for the control simulation (red) is compared to (a) the data (gray), (b) sensitivity tests with diffusive advection (green), (c) $\sigma_h/10$ (blue) and (d) $\epsilon_p/2$ (cyan).

describe the way in which the seasonality diagnostic is used (section 6.1), check its robustness (section 6.2) and then apply it to the SWING2 models (section 6.3).

6.1. The Isotopic Seasonality Diagnostic

[66] Figure 13a shows the subtropical (20°N–30°N) δD seasonality at 350 hPa as a function of tropical (30°S–30°N) annual-mean RH, for the different simulations. As explained earlier, when a moist bias is due to excessively diffusive advection, the seasonality is reversed (green square). This is not the case for the other causes for a moist bias considered in the sensitivity tests (blue and cyan squares). In the δD seasonality versus RH diagram, we will use the slope S between different simulations to diagnose the cause of a moist bias, as illustrated by arrows on Figure 13a. A slope S of the order of −2 to −4‰/% indicates a moist bias that is due to excessively diffusive advection.

[67] We also plot on Figure 13a the approximate position of the data based on AIRS and ACE. The position is subject to large errors for δD because of the sampling mismatch between the observations and monthly mean model outputs. ACE has a much weaker seasonality than MIPAS (P1), so

Table 5. Summary of How Different Causes for a Moist Bias in LMDZ Affects the Isotopic Behavior

	Effect on Isotopic Behavior		
Cause of Moist Bias	Tropical Mean δD	δD Seasonality in the Subtropics	Intraseasonality in the Subtropics
Excessive diffusion during water vapor transport	overestimated in the mid and upper troposphere	underestimated or reversed in the mid and upper troposphere	underestimated variability of δD due to underestimated q-δD slope
Underestimated sub-grid-scale variability of water vapor	overestimated in the mid and upper troposphere	unaffected	overestimated for q but underestimated for δD
Excessive condensate detrainment	overestimated in the upper troposphere with a stronger slope of δD change versus q change.	unaffected	unaffected

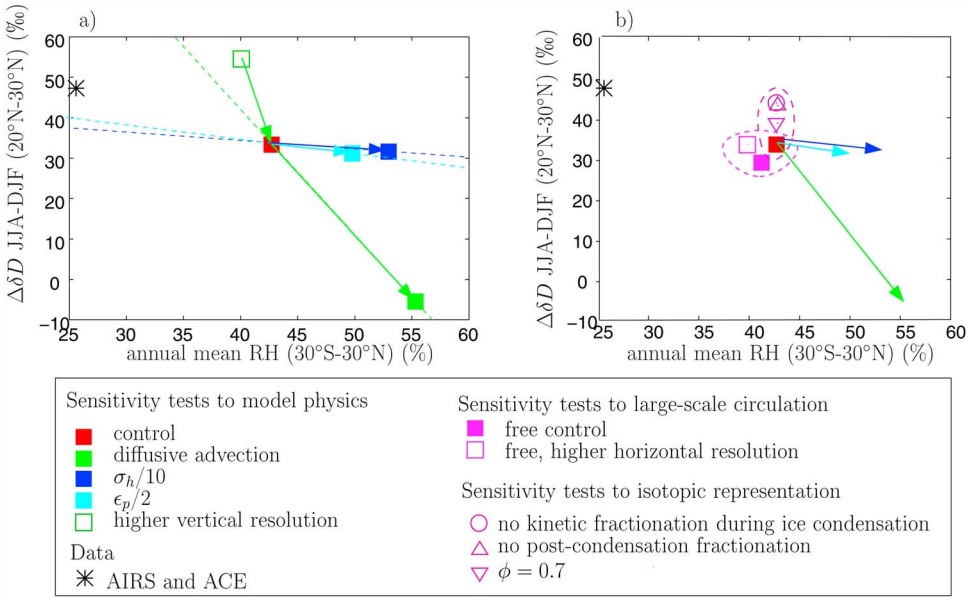

Figure 13. (a) Relationship between annual mean RH at 400 hPa averaged over 30°S–30°N, and seasonal variation (JJA-DJF) of δD at 400 hPa averaged over 20°N–30°N for the different LMDZ simulations (colored squares). The black star indicate corresponding RH and δD values observed by AIRS and ACE-FTS respectively. Note that the comparison with ACE-FTS is qualitative since model outputs cannot be properly collocated with the data on this plot. ACE has a lower δD seasonality than MIPAS, so it likely represent a lower bound. (b) Same as Figure 13a but with some sensitivity tests to the nudging, the horizontal resolution and the isotopic representation. The dashed red and dashed purple circles highlights the proximity to the control of these sensitivity tests.

that ACE likely provides a lower bound for observed δD seasonality. Despite these limitations, based on the consensus that emerged from section 5.3 and Figure 4, the control simulation likely lies between the data and the "diffusive advection" simulation. This suggest that the cause of the moist bias in the control simulation is likely excessively diffusive advection.

[68] The diffusivity of an advection scheme is an intrinsic and unwanted property that cannot be tuned. One way to reduce the diffusion during vertical advection is to increase the vertical resolution. To test whether this solves consistently the moist-bias and the underestimated δD seasonality, we add on Figure 13a the simulation with higher vertical resolution. This simulation is drier and has a stronger seasonality, following a slope similar to that of the "diffusive advection" simulation. This suggests that our δD seasonality diagnostic can detect moist biases that are due to excessive diffusion in a consistent way, be they caused by too diffusive an advection scheme or by to too low a vertical resolution.

6.2. Robustness of the Diagnostic With Respect to Large-Scale Circulation, Isotopic Representation, Diagnostic Definition and Model Physics

[69] Before we apply the slope diagnostic to all GCMs, we check that aspects of the model simulations that are unrelated to the model physics have relatively little impact. First, we recall that sensitivity tests to the nudging and to the horizontal resolution have a comparatively small impact on both RH and δD. On Figure 13b (pink), these tests are very close to the control simulation (dashed red circle). This suggests that differences in RH or in δD seasonality between different models are more likely due the model physics than to differences in the large-scale circulation.

[70] Second, we investigate the impact of differences in the isotopic representation. All SWING2 models use the same equilibrium fractionation coefficients and make similar assumptions during condensation processes (i.e. closed system during liquid condensation and Rayleigh fractionation during ice condensation). Isotopic differences between models can however arise from differences in diffusivity coefficients [*Cappa et al.*, 2003; *Merlivat*, 1978], in kinetic fractionation during ice condensation [*Jouzel and Merlivat*, 1984] or in the representation of isotopic fractionation during rain re-evaporation. Diffusivity coefficients have been shown to affect deuterium excess with very little effect on δD [*Mathieu et al.*, 2002; *Yoshimura et al.*, 2010]. Regarding ice condensation, in all models the supersaturation over ice S_i varies with temperature T following $S_i = 1 - \lambda \cdot T$, where λ is a tunable parameter. Among all SWING2 models, λ varies from 0.003 (e.g. ECHAM, GSM [*Hoffmann et al.*, 1998; *Yoshimura et al.*, 2008]) to 0.005 (HadAM [*Tindall et al.*, 2009]) and is set to 0.004 in LMDZ (Table 2). As an extreme test, we tried $\lambda = 0$ (Figure 13b, purple circle). Although it affects annual mean δD in the upper troposphere, it has a very limited effect on δD seasonality. Regarding isotopic parameterization during rain re-evaporation, there is a wide diversity among models (Table 2). To encompass this diversity, we performed two additional tests with no post-condensation at all [e.g., *Field et al.*, 2010] and with very strong kinetic fractionation respectively (Figure 13b, purple triangles). To represent strong kinetic effects, we change parameter ϕ from 0.9 to 0.7 when calculating the effective

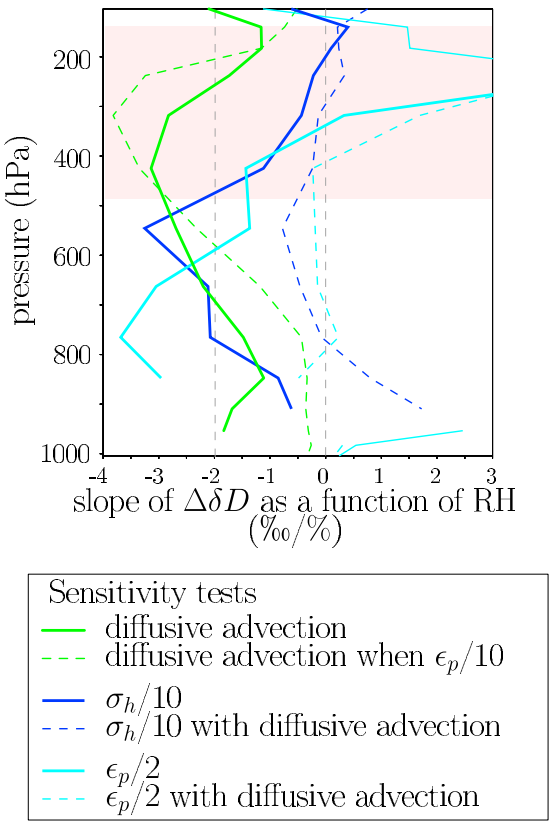

Figure 14. Slope of the seasonal difference in δD versus RH, as in Figure 13, as a function of height for the different sensitivity tests compared to the control. Slopes are shown only where the RH of the two simulations differs by more than 1%. Solid lines: the control simulation and the moist bias simulations are those described in sections 2.1 and 4.1. Dashed lines: same as solid, but both the control and the sensitivity simulations were modified to test the robustness to the model physics. Dashed green: both the control and "diffusive advection" simulations were redone with $\epsilon_p/2$. Dashed blue: both the control and "$\sigma_h/2$" simulations were redone with diffusive advection. Dashed cyan: both the control and "$\epsilon_p/2$" simulations were redone with diffusive advection.

RH around raindrops (h_{eff}) as a function of simulated RH (h) following $h_{eff} = \phi + (1 - \phi) \cdot h$ [*Bony et al.*, 2008; *Risi et al.*, 2010b]. These tests have much smaller impacts than the sensitivity tests to the model physics. Therefore, we conclude that the details of the isotopic implementation is likely not the major factor contributing to the δD seasonality dispersion between models.

[71] We now check the robustness of our diagnostic with respect to altitude. Figure 14 shows the slope S between various pairs of simulations as a function of altitude. The slope between the control and the "diffusive advection" simulation is much more negative than for the other tests from 500 to 150 hPa (solid green). The diagnostic is thus robust with respect to altitude.

[72] We also checked the robustness with respect to the geographical domain. We tested different subtropical domains for δD seasonality (20°N–30°N, 15°N–30°N, 20°N–35°N, 25°N–35°N) and different tropical domains for annual-mean RH (30°S–30°N, 25°S–25°N and 20°S–20°N). The slopes S range within [−3.1, −2.5], [−0.6,0] and [−1.0, −0.3] for the "diffusive advection", "$\sigma_h/10$" and "$\epsilon_p/2$" simulations respectively. Therefore, whatever the choice of the geographical domain, the behavior of the "diffusive advection" can be clearly distinguished from that of the other simulations.

[73] Finally, the robustness of the slope diagnostic with respect to model physics is a necessary condition to apply the diagnostic to all GCMs. The ability to understand the isotopic behavior of the tests with a simple theoretical framework, which involves simple physical processes that are represented in all GCMs, suggests the applicability of these diagnostics to all GCMs. As an additional check, we calculated the slopes S for pairs of simulations with a modified physics. For example, when ϵ_p is divided by two in both the control and "diffusive advection" simulations, the effect of diffusive advection is a deterioration of the seasonality following the same slope S of about −2 to −4‰/% (Figure 14, dashed green). Similarly, when ϵ_p is divided by 2 in both the control and "$\sigma_h/10$" simulations, or when using the diffusive advection scheme in both the control and "$\epsilon_p/2$" simulations, the slopes S characterizing the sensitivity to σ_h and ϵ_p remain much less negative than −2‰/% between 500 and 150 hPa (Figure 14, dashed blue and cyan). Therefore, the isotopic diagnostic is robustly related to the source of the bias and relatively independent of other aspects of model physics.

6.3. Application to SWING2 GCMs

[74] Figure 15b shows the δD seasonality versus RH diagram for the other SWING2 simulations (black markers). As expected, all models are too moist. Models show a very wide spread in δD seasonality, spanning more than 70‰, with variations even in the sign. Isotopic observations can thus discriminate between models despite the large uncertainties in the data sets. The spread in our LMDZ sensitivity tests (about 40‰) is of the same order of magnitude as that in SWING2 models. Most models plot around the line connecting the control and "diffusive advection" simulations (dashed green). Models with the driest troposphere exhibit the strongest (and presumably most realistic: Figure 4) δD seasonality (e.g. Had-AM), while the moistest models exhibit the worst reversed seasonality (e.g. CAM, GSM). This suggests that in many GCMs, excessive diffusion during vertical advection is a likely cause of the moist bias, and the major source of RH dispersion between models.

[75] This result is robust with altitude (Figure 15b): the correlation among models in this diagram is lower than −0.7 from 600 to 250 hPa, and at all these levels the corresponding slope S among models is between than −2 and −4‰/%. This value corresponds to the slope S characterizing the "diffusive advection" simulation at these levels (Figure 15a).

[76] Some GCMs deviate from the "diffusive advection" line (e.g. GISS, MIROC) suggesting that other processes may be responsible for the moist bias in some models. For example, *Wright et al.* [2010] suggest that excessive rainfall evaporation in the GISS model may contribute to its moist bias. However, errors in large-scale circulation are not likely to be the major source of the moist bias and of the spread between models. The small effect of nudging the large-scale circulation in LMDZ is supported by the equally small effect

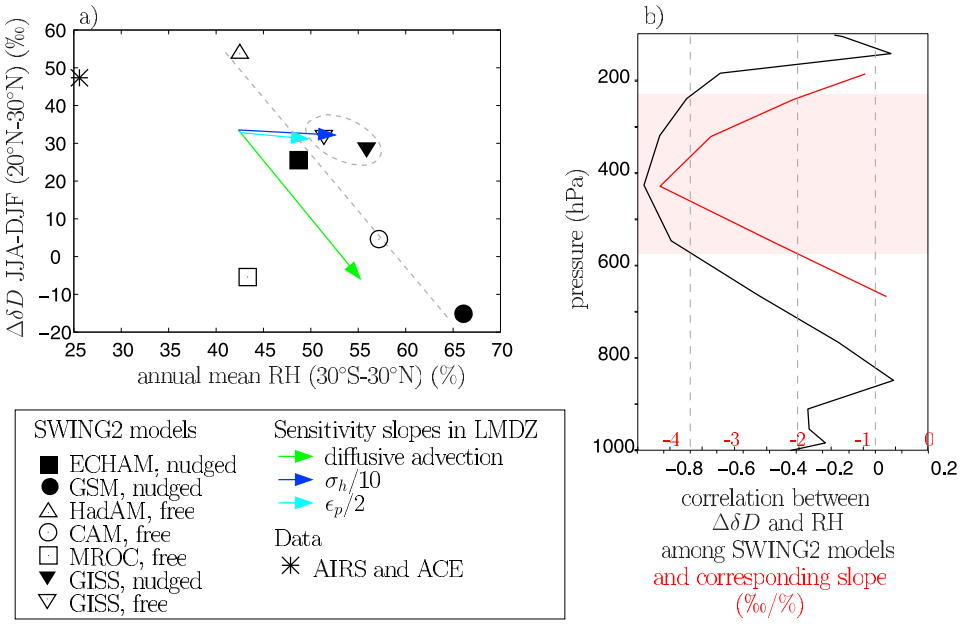

Figure 15. (a) Same as Figure 13 but for the different SWING2 models (black markers), with sensitivity tests to LMDZ physics superimposed as colored arrows. The dashed gray circle highlights the proximity between the free-running and the nudged runs of the GISS model. The dashed gray line visualizes the link between RH and δD seasonality exhibited by most GCMs, following the same slope as for the "diffusive advection" simulation. (b) Correlation (black) and slope (red) of the relationship between subtropical seasonal δD variations and annual mean tropical RH among the SWNG2 models. The slope is plotted only where the correlation is lower than -0.7. The pink shading highlights the range of altitude where the behavior of the "diffusive advection" simulation differs strongly from the other tests (Figure 15a), and where the SWING2 models exhibit a correlation between seasonality and RH lower than -0.7 (Figure 15b).

for the GISS model (dashed gray circle). In addition, the best performing model for RH and δD seasonality is Had-AM, which happens to be run in a free-running mode, while the worst performing model is GSM, which happens to be run in a nudged mode and with the highest horizontal resolution. This further supports the suggestion that the representation of physical processes and advection numerics are larger sources of uncertainties on RH than the large-scale circulation. While it has been shown that nudging might improve the simulation at high latitudes [e.g., *Yoshimura et al.*, 2008; *Risi et al.*, 2010b], a correct large-scale circulation does not guarantee that the tropical and subtropical RH and isotopic distribution are realistic.

7. Conclusion

[77] We show that different processes affecting RH in GCMs impact the water vapor isotopic composition differently. Water vapor isotopic measurements can thus be used as an observational diagnostic to detect and understand causes of RH biases in GCMs. This study proposes an approach to practically do so. The isotopic sensitivity to various physical processes is first understood using sensitivity tests and a simple framework. An isotopic diagnostic based on observations is then designed, and its robustness with respect to the data set used and other aspects of the model physics and isotopic representation is checked. This diagnostic is finally applied to a wider range of models to diagnose the reason for their bias.

[78] As an example, in this study we aim at understanding the reasons for the moist bias in the tropical mid and upper troposphere that has persisted in GCMs for more than a decade. We show that the isotopic seasonality in the subtropics can robustly discriminate simulations in which the moist bias is due to excessively diffusive vertical advection. Applying this isotopic diagnostic to an ensemble of GCMs suggests that excessive diffusion during vertical advection is the most frequent cause of moist bias in GCMs. However, our approach bears some limitations: (1) the lack of validation of upper-tropospheric isotopic data sets, (2) the limited number of our sensitivity tests to the model physics, leaving some other possible sources of moist bias unexplored, (3) the limited subset of GCMs with an isotopic representation and (4) the absence of similar sensitivity tests in the other isotopic GCMs to further check the universality of our diagnostic.

[79] Although it has long been recognized that the large-scale circulation controls the spatial distribution of RH to first order [*Sherwood*, 1996; *Pierrehumbert and Roca*, 1998], our study highlights the importance of uncertainties related to parameterized processes controlling RH and advection numerics. If excessive diffusion during vertical advection is indeed the most frequent cause of moist bias in GCMs, this problem can be solved by improving the advection scheme, or alternatively by increasing the vertical resolution. This is consistent with sensitivity to vertical resolutions in other GCMs [*Pope et al.*, 2001; *Roeckner*

et al., 2006], and supports the importance of vertical resolution [*Tompkins and Emanuel*, 2007]. It would be interesting to apply our isotopic diagnostic to more models, in particular those for which other causes for the moist biases have been hypothesized but which did not participate in SWING2 (e.g. Geophysical Fluid Dynamics Laboratory model [*Chung et al.*, 2011]).

[80] **Acknowledgments.** We thank Debra Wunch, Vanessa Sherlock, Nicholas Deutscher, David Griffith, Paul Wennberg, Kimberly Strong, Sabine Barthlott, Frank Hase, Omaira García, Dan Smale, Emmanuel Mahieu, Justus Notholt, Thorsten Warneke and Geofrey Toon for their roles in acquiring the ground-based remote-sensing data and developing the retrievals, for making the data available, for helping with the data processing and for their useful advice to develop the rigorous model-data comparison methodology used in this paper. We thank David Sayres for providing in situ and aircraft data. We also thank Debra Wunch, Vanessa Sherlock, Nicholas Deutscher, Paul Wennberg and Kimberly Strong for detailed comments on the manuscript. Level-1b data of MIPAS have been provided by ESA. The ACE mission is supported mainly by the Canadian Space Agency. We thank the Anderson Group at Harvard University for providing ICOS and Hoxotope in situ aircraft data. We acknowledge all FTIR activities as in P1. The mid-infrared FTIR retrievals have been performed in the framework of the project MUSICA (http://www.imk-asf.kit.edu/english/musica), which is funded by the European Research Council under the European Community's Seventh Framework Programme (FP7/2007–2013)/ERC grant agreement 256961. We thank Omaira García who was in charge of the FTIR activities at Izaña. We thank all SWING2 members for producing and making available their model outputs. SWING2 was supported by the Isotopic Hydrology Programme at the International Atomic Energy Agency (more information on http://people.su.se/∼cstur/SWING2). We thank Françoise Vimeux for discussions. This work was supported by NASA Energy and Water-cycle Study (07-NEWS07-0020) and NASA Atmospheric Composition program (NNX08AR23G). We thank anonymous reviewers for their constructive comments.

References

Allan, R., M. A. Ringer, and A. Slingo (2003), Evaluation of moisture in the Hadley Centre climate model using simulations of HIRS water-vapour channel radiances, *Q. J. R. Meteorol. Soc.*, *129*(595), 3371–3389.

Angert, A., J.-E. Lee, and D. Yakir (2008), Seasonal variations in the isotopic composition of near-surface water vapour in the eastern Mediterranean, *Tellus, Ser. B*, *60*(4), 674–684.

Arakawa, A., and W. Shubert (1974), Interactions of cumulus cloud ensemble with the large-scale environment. Part I, *J. Atmos. Sci.*, *31*, 671–701.

Aumann, H. H., et al. (2003), AIRS/AMSU/HSB on the Aqua mission: Design, science objectives, data products, and processing systems, *IEEE Trans. Geosci. Remote Sens.*, *41*, 253–264.

Betts, A. K. (2000), Idealized model for equilibrium boundary layer over land, *J. Hydrometeorol.*, *1*, 507–523.

Bony, S., and J. Dufresne (2005), Marine boundary layer clouds at the heart of tropical cloud feedback uncertainties in climate models, *Geophys. Res. Lett.*, *32*, L20806, doi:10.1029/2005GL023851.

Bony, S., and K. A. Emanuel (2001), A parameterization of the cloudiness associated with cumulus convection: Evaluation using TOGA COARE data, *J. Atmos. Sci.*, *58*, 3158–3183.

Bony, S., J.-L. Dufresne, H. Le Treut, J.-J. Morcrette, and C. Senior (2004), On dynamic and thermodynamic components of cloud changes, *Clim. Dyn.*, *22*, 71–86.

Bony, S., et al. (2006), How well do we understand and evaluate climate change feedback processes?, *J. Clim.*, *19*, 3445–3482.

Bony, S., C. Risi, and F. Vimeux (2008), Influence of convective processes on the isotopic composition (δ^{18}O and δD) of precipitation and water vapor in the tropics: 1. Radiative-convective equilibrium and TOGA-COARE simulations, *J. Geophys. Res.*, *113*, D19305, doi:10.1029/2008JD009942.

Brogniez, C., R. Roca, and L. Picon (2005), Evaluation of the distribution of subtropical free tropospheric humidity in AMIP-2 simulations using METEOSAT water vapor channel data, *Geophys. Res. Lett.*, *32*, L19708, doi:10.1029/2005GL024341.

Brown, D., J. Worden, and D. Noone (2008), Comparison of atmospheric hydrology over convective contnental regions using water vapor isotope measurements from space, *J. Geophys. Res.*, *113*, D15124, doi:10.1029/2007JD009676.

Cappa, C., M. Hendricks, D. DePaolo, and R. Cohen (2003), Isotopic fractionation of water during reevaporation, *J. Geophys. Res.*, *108*(D16), 4525, doi:10.1029/2003JD003597.

Chen, C., E. Roeckner, and B. J. Soden (1996), A comparison of satellite observations and model simulations of column-integrated moisture and upper-tropospheric humidity, *J. Clim.*, *9*, 1561–1585.

Chen, M., R. B. Rood, and W. G. Read (1998), Upper tropospheric water vapor from GEOS reanalysis and UARS MLS observation, *J. Geophys. Res.*, *103*(D16), 19,587–19,594.

Chung, E.-S., B. J. Soden, B.-J. Sohn, and J. Schmetz (2011), Model-simulated humidity bias in the upper troposphere and its relation to the large-scale circulation, *J. Geophys. Res.*, *116*, D10110, doi:10.1029/2011JD015609.

Craig, H. (1961), Isotopic variations in meteoric waters, *Science*, *133*, 1702–1703.

Dansgaard, W. (1964), Stable isotopes in precipitation, *Tellus*, *16*, 436–468.

Derbyshire, S. H., I. Beau, P. Bechtold, J.-Y. Grandpeix, J.-M. Piriou, J.-L. Redelsperger, and P. M. M. Soares (2004), Sensitivity of moist convection to environmental humidity, *Q. J. R. Meteorol. Soc.*, *130*(604), 3055–3079.

Dessler, A. E., and S. C. Sherwood (2000), Simulations of tropical upper tropospheric humidity, *J. Geophys. Res.*, *105*(D15), 20,155–20,263.

Ehhalt, D. H., F. Rohrer, and A. Fried (2005), Vertical profiles of HDO/H_2O in the troposphere, *J. Geophys. Res.*, *110*, D13301, doi:10.1029/2004JD005569.

Emanuel, K. A. (1991), A scheme for representing cumulus convection in large-scale models, *J. Atmos. Sci.*, *48*, 2313–2329.

Emanuel, K. A., and M. Zivkovic-Rothman (1999), Development and evaluation of a convection scheme for use in climate models, *J. Atmos. Sci.*, *56*, 1766–1782.

Emanuel, K., D. Neelin, and C. Bretherton (1994), On large-scale circulations in convecting atmospheres, *Q. J. R. Meteorol. Soc.*, *120*, 1111–1143.

Fetzer, E. J., B. H. Lambrigtsen, A. Eldering, H. H. Aumann, and M. T. Chahine (2006), Biases in total precipitable water vapor climatologies from Atmospheric Infrared Sounder and Advanced Microwave Scanning Radiometer, *J. Geophys. Res.*, *111*, D09S16, doi:10.1029/2005JD006598.

Field, R. D., D. B. A. Jones, and D. P. Brown (2010), The effects of post-condensation exchange on the isotopic composition of water in the atmosphere, *J. Geophys. Res.*, *115*, D24305, doi:10.1029/2010JD014334.

Folkins, I., and R. Martin (2005), The vertical structure of tropical convection and its impact on the budgets of water vapor and ozone, *J. Atmos. Sci.*, *62*, 1560–1573.

Frankenberg, C., et al. (2009), Dynamic processes governing lower-tropospheric HDO/H_2O ratios as observed from space and ground, *Science*, *325*, 1374–1377.

Galewsky, J., and J. V. Hurley (2010), An advection-condensation model for subtropical water vapor isotopic ratios, *J. Geophys. Res.*, *115*, D16116, doi:10.1029/2009JD013651.

Gao, J., V. Masson-Delmotte, T. Yao, C. Risi, G. Hoffmann, and L. Tian (2010), Precipitation water stable isotopes in the south Tibetan Plateau: Observations and modelling, *J. Clim.*, *24*, 3161–3178, doi:10.1175/2010JCLI3736.1.

Gates, W. L. (1992), AMIP: The Atmospheric Model Intercomparison Project, *Bull. Am. Meteorol. Soc.*, *73*, 1962–1970.

Godunov, S. K. (1959), Finite-difference methods for the numerical computations of equations of gas dynamics, *Math. Sb.*, *7*, 271–290.

Grandpeix, J. Y., V. Phillips, and R. Tailleux (2004), Improved mixing representation in Emanuel's convection scheme, *Q. J. R. Meteorol. Soc.*, *130*, 3207–3222.

Hoffmann, G., M. Werner, and M. Heimann (1998), Water isotope module of the ECHAM atmospheric general circulation model: A study on timescales from days to several years, *J. Geophys. Res.*, *103*, 16,871–16,896.

Hourdin, F., and A. Armengaud (1999), The use of finite-volume methods for atmospheric advection of trace species. Part I: Test of various formulations in a General Circulation Model, *Mon. Weather Rev.*, *127*, 822–837.

Hourdin, F., et al. (2006), The LMDZ4 general circulation model: Climate performance and sensitivity to parametrized physics with emphasis on tropical convection, *Clim. Dyn.*, *27*, 787–813.

John, V. O., and B. J. Soden (2007), Temperature and humidity biases in global climate models and their impact on climate feedbacks, *Geophys. Res. Lett.*, *34*, L18704, doi:10.1029/2007GL030429.

Johnson, L. R., Z. Sharp, J. Galewsky, M. Strong, P. Gupta, D. Baer, and D. Noone (2011), Hydrogen isotope measurements of water vapor and a correction for laser instrument measurement bias at low water vapor concentrations: Applications to measurements from Mauna Loa Observatory, Hawaii, *Rapid Commun. Mass Spectrom.*, *25*, 608–616.

Jouzel, J., and L. Merlivat (1984), Deuterium and oxygen 18 in precipitation: modeling of the isotopic effects during snow formation, *J. Geophys. Res.*, *89*, 11,749–11,757.

Kalnay, E., et al. (1996), The NCEP/NCAR 40-year reanalysis project, *Bull. Am. Meteorol. Soc.*, *77*, 437–470.

Kurita, N., D. Noone, C. Risi, G. A. Schmidt, H. Yamada, and K. Yoneyama (2011), Intraseasonal isotopic variation associated with the Madden-Julian Oscillation, *J. Geophys. Res.*, *116*, D24101, doi:10.1029/2010JD015209.

Lawrence, J. R., S. D. Gedzelman, D. Dexheimer, H.-K. Cho, G. D. Carrie, R. Gasparini, C. R. Anderson, K. P. Bowman, and M. I. Biggerstaff (2004), Stable isotopic composition of water vapor in the tropics, *J. Geophys. Res.*, *109*, D06115, doi:10.1029/2003JD004046.

Lawrence, M. G., and M. Salzmann (2008), On interpreting studies of tracer transport by deep cumulus convection and its effects on atmospheric chemistry, *Atmos. Chem. Phys.*, *8*(20), 6037–6050.

Lee, J.-E., and I. Fung (2008), "Amount effect" of water isotopes and quantitative analysis of post-condensation processes, *Hydrol. Processes*, *22*(1), 1–8.

Lee, J.-E., I. Fung, D. DePaolo, and C. C. Fennig (2007), Analysis of the global distribution of water isotopes using the NCAR atmospheric general circulation model, *J. Geophys. Res.*, *112*, D16306, doi:10.1029/2006JD007657.

Luo, Z., and W. B. Rossow (2004), Characterizing tropical cirrus life cycle, evolution, and interaction with upper-tropospheric water vapor using Lagrangian trajectory analysis of satellite observations, *J. Clim.*, *17*, 4541–4563.

Majoube, M. (1971a), Fractionnement en O18 entre la glace et la vapeur d'eau, *J. Chim. Phys.*, *68*, 625–636.

Majoube, M. (1971b), Fractionnement en Oxygéne 18 et en Deutérium entre l'eau et sa vapeur, *J. Chim. Phys.*, *10*, 1423–1436.

Marti, O., et al. (2005), The new IPSL climate system model: IPSL-CM4, technical report, IPSL, Paris.

Mathieu, R., D. Pollard, J. Cole, J. W. C. White, R. S. Webb, and S. L. Thompson (2002), Simulation of stable water isotope variations by the GENESIS GCM for modern conditions, *J. Geophys. Res.*, *107*(D4), 4037, doi:10.1029/2001JD900255.

Meehl, G. A., K. Covey, T. Delworth, M. Latif, B. McAvaney, J. F. B. Mitchell, R. J. Stouffer, and K. Taylor (2007), The WCRP CMIP3 multimodel dataset: A new era in climate change research, *Bull. Am. Meteorol. Soc.*, *7*, 1383–1394.

Merlivat, L. (1978), Molecular diffusivities of H2O16, HDO16, and H2O18 in gases, *J. Chem. Phys.*, *69*, 2864–2871.

Merlivat, L., and G. Nief (1967), Fractionnement isotopique lors des changements d'états solide-vapeur et liquide-vapeur de l'eau à des températures inférieures à 0°C, *Tellus*, *19*, 122–127.

Moyer, E. J., F. W. Irion, Y. L. Yung, and M. R. Gunson (1996), ATMOS stratospheric deuterated water and implications for troposphere-stratosphere transport, *Geophys. Res. Lett.*, *23*, 2385–2388.

Nassar, R., P. F. Bernath, C. D. Boone, A. Gettelman, S. D. McLeod, and C. P. Rinsland (2007), Variability in HDO/H_2O abundance ratio in the tropical tropopause layer, *J. Geophys. Res.*, *112*, D21305, doi:10.1029/2007JD008417.

Noone, D., et al. (2011), Properties of air mass mixing and humidity in the subtropics from measurements of the D/H isotope ratio of water vapor at the Mauna Loa Observatory, *J. Geophys. Res.*, *116*, D22113, doi:10.1029/2011JD015773.

Pierce, D. W., T. P. Barnett, E. J. Fetzer, and P. J. Gleckler (2006), Three-dimensional tropospheric water vapor in coupled climate models compared with observations from the AIRS satellite system, *Geophys. Res. Lett.*, *33*, L21701, doi:10.1029/2006GL027060.

Pierrehumbert, R. T. (1998), Lateral mixing as a source of subtropical water vapor, *Geophys. Res. Lett.*, *25*(2), 151–154.

Pierrehumbert, R. T., and R. Roca (1998), Evidence for control of Atlantic subtropical humidity by large scale advection, *Geophys. Res. Lett.*, *25*, 4537–4540.

Pope, V. D., J. A. Pamment, D. R. Jackson, and A. Slingo (2001), The representation of water vapor and its dependence on vertical resolution in the Hadley Centre Climate Model, *J. Clim.*, *14*, 3065–3085.

Randall, D., et al. (2007), Climate models and their evaluation, in *Climate Change 2007: The Physical Science Basis. Contribution of Working Group I to the Fourth Assessment Report of the Intergovernmental Panel on Climate Change*, edited by S. Solomon et al., pp. 591–662, Cambridge Univ. Press, Cambridge, U. K.

Redelsperger, J.-L., D. B. Parsons, and F. Guichard (2002), Recovery processes and factors limiting cloud-top height following the arrival of a dry intrusion observed during TOGA COARE, *J. Atmos. Sci.*, *59*, 2438–2457.

Risi, C., S. Bony, and F. Vimeux (2008), Influence of convective processes on the isotopic composition ($\delta^{18}O$ and δD) of precipitation and water vapor in the tropics: 2. Physical interpretation of the amount effect, *J. Geophys. Res.*, *113*, D19306, doi:10.1029/2008JD009943.

Risi, C., S. Bony, F. Vimeux, M. Chong, and L. Descroix (2010a), Evolution of the water stable isotopic composition of the rain sampled along Sahelian squall lines, *Q. J. R. Meteorol. Soc.*, *136*(S1), 227–242.

Risi, C., S. Bony, F. Vimeux, and J. Jouzel (2010b), Water stable isotopes in the LMDZ4 General Circulation Model: Model evaluation for present day and past climates and applications to climatic interpretation of tropical isotopic records, *J. Geophys. Res.*, *115*, D12118, doi:10.1029/2009JD013255.

Risi, C., et al. (2012), Process-evaluation of tropospheric humidity simulated by general circulation models using water vapor isotopologues: 1. Comparison between models and observations, *J. Geophys. Res.*, *117*, D05303, doi:10.1029/2011JD016621.

Roca, R., L. Picon, M. Desbois, H. Le Treut, and J.-J. Morcrette (1997), Direct comparison of Meteosat water vapor channel data and general circulation model results, *Geophys. Res. Lett.*, *24*(2), 147–150.

Roeckner, E., R. Brokopf, M. Esch, M. Giorgetta, S. Hagemann, L. Kornblueh, E. Manzini, U. Schlese, and U. Schulzweida (2006), Sensitivity of simulated climate to horizontal and vertical resolution in the ECHAM5 atmosphere model, *J. Clim.*, *19*(16), 3771–3791.

Salathe, E. J., and D. Chester (1995), Variability of moisture in the upper troposphere as inferred from TOVS satellite observations in the ECMWF model analyses in 1989, *J. Clim.*, *8*, 120–132.

Sayres, D. S., L. Pfister, T. F. Hanisco, E. J. Moyer, J. B. Smith, J. M. S. Clair, A. S. O'Brien, M. F. Witinski, M. Legg, and J. G. Anderson (2010), Influence of convection on the water isotopic composition of the tropical tropopause layer and tropical stratosphere, *J. Geophys. Res.*, *115*, D00J20, doi:10.1029/2009JD013100.

Schmidt, G., A. LeGrande, and G. Hoffmann (2007), Water isotope expressions of intrinsic and forced variability in a coupled ocean-atmosphere model, *J. Geophys. Res.*, *112*, D10103, doi:10.1029/2006JD007781.

Schneider, M., K. Yoshimura, F. Hase, and T. Blumenstock (2010), The ground-based FTIR network's potential for investigating the atmospheric water cycle, *Atmos. Chem. Phys.*, *10*, 3427–3442.

Schneider, T., K. L. Smith, P. A. O'Gorman, and C. C. Walker (2006), A climatology of tropospheric zonal-mean water vapor fields and fluxes in isentropic coordinates, *J. Clim.*, *19*(22), 5918–5933.

Sherwood, S. C. (1996), Maintenance of the free tropospheric tropical water vapor distribution. Part II: Simulation of large-scale advection, *J. Clim.*, *11*, 2919–2934.

Sherwood, S., and C. Meyer (2006), The general circulation and robust relative humidity, *J. Clim.*, *19*(24), 6278–6290.

Sherwood, S. C., W. Ingram, Y. Tsushima, M. Satoh, M. Roberts, P. L. Vidale, and P. A. O'Gorman (2010), Relative humidity changes in a warmer climate, *J. Geophys. Res.*, *115*, D09104, doi:10.1029/2009JD012585.

Slingo, J. M. (1980), A cloud parametrization scheme derived from GATE data for use with a numerical model, *Q. J. R. Meteorol. Soc.*, *106*(450), 747–770.

Sobel, A. H., and C. S. Bretherton (2000), Modeling tropical precipitation in a single column, *J. Clim.*, *13*, 4378–4392.

Soden, B. J., and C. Bretherton (1994), Evaluation of water vapor distribution in general circulation models using satellite observations, *J. Geophys. Res.*, *99*(D1), 1187–1210, doi:10.1029/93JD02912.

Soden, B. J., and I. M. Held (2006), An assessment of climate feedbacks in coupled ocean?atmosphere models, *J. Clim.*, *19*, 3354–3360, doi:10.1175/JCLI3799.1.

Steinwagner, J., S. Fueglistaler, G. Stiller, T. von Clarmann, M. Kiefer, P.-P. Borsboom, A. van Delden, and T. Röckmann (2010), Tropical dehydration processes constrained by the seasonality of stratospheric deuterated water, *Nat. Geosci.*, *3*, 262–266, doi:10.1038/NGEO822.

Stewart, M. K. (1975), Stable isotope fractionation due to evaporation and isotopic exchange of falling waterdrops: Applications to atmospheric processes and evaporation of lakes, *J. Geophys. Res.*, *80*, 1133–1146.

Tindall, J. C., P. Valdes, and L. C. Sime (2009), Stable water isotopes in HadCM3: Isotopic signature of El Niño–Southern Oscillation and the tropical amount effect, *J. Geophys. Res.*, *114*, D04111, doi:10.1029/2008JD010825.

Tompkins, A. M., and K. Emanuel (2007), The vertical resolution sensitivity of simulated equilibrium temperature and water-vapour profiles, *Q. J. R. Meteorol. Soc.*, *126*(565), 1219–1238.

Uemura, R., Y. Matsui, K. Yoshimura, H. Motoyama, and N. Yoshida (2008), Evidence of deuterium-excess in water vapour as an indicator of ocean surface conditions, *J. Geophys. Res.*, *113*, D19114, doi:10.1029/2008JD010209.

Uppala, S., et al. (2005), The ERA-40 re-analysis, *Q. J. R. Meteorol. Soc.*, *131*, 2961–3012.

Van Leer, B. (1977), Towards the ultimate conservative difference scheme: IV. A new approach to numerical convection, *J. Comput. Phys.*, *23*, 276–299.

Vimeux, F., G. Tremoy, C. Risi, and R. Gallaire (2011), A strong control of the South American SeeSaw on the intraseasonal variability of the isotopic composition of precipitation in the Bolivian Andes, *Earth. Planet. Sci. Lett.*, *307*(1–2), 47–58.

Webster, C. R., and A. J. Heymsfield (2003), Water isotope ratios D/H, $^{18}O/^{16}O$, $^{18}O/^{16}O$ in and out of clouds map dehydration pathways, *Science*, *302*, 1742–1746.

Wetzel, P. J., S. Argentini, and A. Boone (1996), Role of land surface in controlling daytime cloud amount: Two case studies in the GCIP-SW area, *J. Geophys. Res.*, *101*, 7359–7370.

Worden, J., D. Noone, and K. Bowman (2007), Importance of rain evaporation and continental convection in the tropical water cycle, *Nature*, *445*, 528–532.

Wright, J. S., A. H. Sobel, and G. A. Schmidt (2009), The influence of condensate evaporation on water vapor and its stable isotopes in a GCM, *Geophys. Res. Lett.*, *36*, L12804, doi:10.1029/2009GL038091.

Wright, J. S., A. Sobel, and J. Galewsky (2010), Diagnosis of zonal mean relative humidity changes in a warmer climate, *J. Clim.*, *23*, 4556–4569, doi:10.1175/2010JCLI3488.1.

Wunch, D., et al. (2010), Calibration of the total carbon column observing network using aircraft profile data, *Atmos. Meas. Tech.*, *3*, 1351–1362, doi:10.5194/amt-3-1351-2010.

Yoshimura, K., M. Kanamitsu, D. Noone, and T. Oki (2008), Historical isotope simulation using reanalysis atmospheric data, *J. Geophys. Res.*, *113*, D19108, doi:10.1029/2008JD010074.

Yoshimura, K., M. Kanamitsu, and M. Dettinger (2010), Regional downscaling for stable water isotopes: A case study of an atmospheric river event, *J. Geophys. Res.*, *115*, D18114, doi:10.1029/2010JD014032.

Zhang, C., B. Mapes, and B. J. Soden (2003), Bimodality in tropical water vapour, *Q. J. R. Meteorol. Soc.*, *129*(594), 2847–2866.

P. Bernath, Department of Chemistry, University of York, York YO10 5DD, UK.

S. Bony, LMD/IPSL, CNRS, Case Postale 99, 4 Place Jussieu, F-75252 Paris, France.

D. Brown, D. Noone, and C. Risi, Department of Atmospheric and Oceanic Sciences, University of Colorado at Boulder, Bldg. 318, 216 UCB, Main Campus, Boulder, CO 80309, USA. (camille.risi@colorado.edu)

C. Frankenberg and J. Worden, Jet Propulsion Laboratory, California Institute of Technology, 4800 Oak Grove Dr., Pasadena, CA 91109, USA.

B. Funke, Instituto de Astrofísica de Andalucía, Apdo. 3004, E-18008 Granada, Spain.

M. Kiefer, M. Schneider, and G. Stiller, IMK-ASF, Institute for Meteorology and Climate Research, Karlsruhe Institute of Technology, PO Box 3640, D-76021 Karlsruhe, Germany.

J. Lee, Korea Polar Research Institute, Incheon 406-840, South Korea.

C. Sturm, Department of Geology and Geochemistry, Stockholm University, SE-10961 Stockholm, Sweden.

K. Walker, Department of Physics, University of Toronto, 60 St. George St., Toronto, ON M5S 1A7, Canada.